Upscaling and Gridding of Fine Scale Geological Models for Flow Simulation

Louis J. Durlofsky

Department of Petroleum Engineering, Stanford University,
Stanford, CA 94305-2220 USA

Abstract

A variety of approaches for gridding and upscaling of detailed geocellular models for flow simulation are reviewed. Local, extended local, global and quasi global techniques for the calculation of equivalent permeability and transmissibility are discussed. Specialized procedures for permeability upscaling in the vicinity of wells are also described. Flow-based grid generation techniques, in which a curvilinear grid is introduced to resolve the effects of permeability connectivity, are described along with procedures for computing upscaled properties for such grids. Coarse scale simulation results generated using many of these upscaling techniques are presented. These results illustrate the capabilities of existing upscaling procedures and demonstrate the levels of accuracy attainable using the various approaches.

1 Introduction

Typical reservoir simulators can handle on the order of $10^5 - 10^6$ simulation cells. The exact number will vary considerably depending on the type of simulation to be performed (dead oil, black oil, compositional) and the available computer hardware. For many types of models, production version simulations with over 10^6 cells are still not performed routinely. Geological characterizations, by contrast, typically contain on the order of $10^7 - 10^8$ cells. These models, which are referred to as fine grid models, geostatistical models or simply geocellular models, represent geological variation on very fine scales vertically, though their areal resolution is still relatively coarse. For example, a typical geostatistical model might contain layering of thickness 1 ft or less, though cell sizes in the areal direction might be about 50 - 100 ft. Thus, fine

1

grid geological descriptions can be expected to grow further, so the need for reliable upscaling techniques will continue.

Another issue of considerable importance is the need for the assessment of risk and uncertainty in reservoir performance. Nearly every aspect of the reservoir characterization contains some degree of uncertainty, so predictions are necessarily of a statistical character. The uncertainty in reservoir performance can be gauged by simulating a number of different geological realizations or scenarios. Thousands of such runs may be required to cover the range of parameter variation. It is not computationally feasible (or desirable) to perform these simulations on the fine grid model. Significantly upscaled models are required if a full assessment of project risk and uncertainty is to be accomplished. These models should ideally be even coarser than the $O(10^5 - 10^6)$ grid block models referred to above. In addition, if thousands of coarse models are to be simulated, the upscaling must be highly automated.

Different upscaling procedures are appropriate in different situations. The ideal procedure to use on a particular problem depends on the simulation question being addressed, the production mechanism, and the level of detail that can be accommodated in the coarse model. For a problem involving primary production with only oil being produced, the coarse model should correctly capture the effects of near-well heterogeneity as well as the general large scale flow response of the reservoir. For scenarios involving displacement of oil by water or gas, it may be important to accurately capture the effects of key flow paths between injection and production wells. This may require the use of specialized gridding procedures.

Following the description of the governing equations below, we classify upscaling techniques in terms of the types of parameters that are upscaled (single or two-phase flow parameter upscaling). For moderate degrees of coarsening, single-phase upscaling techniques often provide acceptable results, particularly when used in conjunction with specialized (flow-based) coarse grids. At higher degrees of coarsening, some type of relative permeability upscaling is also generally required. In order to maintain focus, this review will cover only techniques for single-phase upscaling and for the generation of coarse grids. The calculation of upscaled relative permeabilities is an important topic that has been addressed in several recent reviews and comparison studies; see for example Christie [18], Barker and Thibeau [8], Barker and Dupouy [7], Darman *et al.* [20] and Gerritsen and Durlofsky [40]. Recent reviews on upscaling with a focus closer to that of this review include those by Wen and Gómez-Hernández [90], Renard and de Marsily [78] and Farmer [37]. Our emphasis here will be on methods implemented for structured grids, though many of the methods discussed could be readily adapted to unstructured grids.

This review proceeds as follows. In §2 we present the equations governing single and two-phase flow on the fine scale and then describe some ways in which upscaling procedures can be classified. We present the coarse scale pressure equation and introduce the upscaled permeability tensor $\mathbf{k}^*$ in §3. Analytical upscaling proce-

dures are then briefly considered. In §4 we discuss numerical methods for the local calculation of $\mathbf{k}^*$ or upscaled transmissibility T^*. We consider various boundary conditions for these calculations and describe different post-processing procedures for computing $\mathbf{k}^*$ from the local solutions. Next, we describe extended local upscaling techniques (e.g., the use of border regions) and the determination of $\mathbf{k}^*$ and T^* for irregular coarse grid control volumes. Upscaling in the vicinity of wells (which also requires the calculation of an upscaled well index) is also considered. In §5 we discuss global and quasi global coarsening procedures. These include the recently developed local-global techniques, in which global coarse scale solutions are used to guide the local upscaling calculations. Flow-based and elliptic grid generation procedures are considered in §6. We briefly discuss approaches for assessing the quality of the upscaled model in §6.3. In §7, numerical results for many of the procedures described in previous sections are presented. Results using local, extended local and local-global techniques are included. We also present results using near-well upscaling and flow-based gridding. We conclude in §8 with a summary and a discussion of potential future directions for research in the area of upscaling. We note that this review represents an update of an earlier paper presented at the 7th International Forum on Reservoir Simulation in 2003 (Durlofsky [25]).

2 Fine scale equations and classifications of upscaling procedures

We now consider the equations describing single and two-phase flow on the fine scale. These equations are strictly appropriate for use with a fully resolved or fine scale geocellular model; i.e., one in which no upscaling has been performed.

2.1 Single-phase flow equations

The equation governing single-phase flow in the absence of gravity is formed by combining Darcy's law

$$\mathbf{u} = -\frac{1}{\mu}\,\mathbf{k}\cdot\nabla p, \tag{1}$$

with a statement of mass conservation

$$\frac{\partial}{\partial t}\left(\phi\rho\right) + \nabla\cdot\left(\rho\mathbf{u}\right) + \tilde{m} = 0. \tag{2}$$

The resulting equation, referred to as the pressure equation, is given by:

$$\frac{\partial}{\partial t}\left(\phi\rho\right) - \nabla\cdot\left(\frac{\rho}{\mu}\mathbf{k}\cdot\nabla p\right) + \tilde{m} = 0. \tag{3}$$

In Eqs. (1)-(3), $\mathbf{u}$ is the Darcy velocity, μ is viscosity, $\mathbf{k}$ is the (symmetric positive definite) permeability tensor, p is pressure, t is time, ϕ is porosity, ρ is density and $\tilde{m}$ is the source/sink term (positive for production) expressed as a mass flow rate per unit volume.

Upscaling procedures are generally formulated based on a simplified form of Eq. (3). Specifically, if we assume that the fluid and rock are incompressible (i.e., ρ does not vary in space or time and $\partial\phi/\partial t = 0$), we obtain a simplified pressure equation:

$$\nabla \cdot \left(\frac{1}{\mu} \, \mathbf{k} \cdot \nabla p \right) = \tilde{q}, \tag{4}$$

where $\tilde{q} = \tilde{m}/\rho$ is the volumetric source term. The equations above can be modified to account for the effects of gravity by replacing p with the potential $\Phi = p - \rho g z$, where g is the gravitational acceleration and the z axis points vertically downwards (in the direction of gravity), as is the convention for most reservoir simulators.

2.2 Two-phase flow equations

The equations describing two-phase flow on the fine scale can again be formed by combining Darcy's law with a statement of mass conservation. In this case, in the absence of gravity, Darcy's law can be expressed as:

$$\mathbf{u}_j = -\frac{k_{rj}}{\mu_j} \mathbf{k} \cdot \nabla p_j, \tag{5}$$

where the subscript j refers to the phase ($j = w$ for water and $j = o$ for oil) and k_{rj} is the relative permeability to phase j. Mass conservation is given by:

$$\frac{\partial}{\partial t} \left(\phi \rho_j S_j \right) + \nabla \cdot \left(\rho_j \mathbf{u}_j \right) + \tilde{m}_j = 0, \tag{6}$$

where S_j is the saturation (volume fraction) of phase j. If we assume that $\partial\phi/\partial t = 0$, that ρ_j does not vary in time or space, and that capillary pressure (p_c) is negligible; i.e., $p_c(S_w) = p_o - p_w = 0$, we obtain:

$$\nabla \cdot \mathbf{u}_t = -\tilde{q}_t, \tag{7}$$

where $\tilde{q}_j = \tilde{m}_j/\rho_j$ and the total volumetric source term is $\tilde{q}_t = \tilde{q}_w + \tilde{q}_o$. The total Darcy velocity $\mathbf{u}_t$ is given by:

$$\mathbf{u}_t = \mathbf{u}_w + \mathbf{u}_o = -\mathbf{k} \left(\frac{k_{rw}}{\mu_w} + \frac{k_{ro}}{\mu_o} \right) \cdot \nabla p. \tag{8}$$

The water velocity $\mathbf{u}_w$ can now be expressed as $\mathbf{u}_w = f(S_w)\mathbf{u}_t$ where $f(S_w)$ is the usual Buckley-Leverett fractional flow function. Inserting this form for $\mathbf{u}_w$ in Eq. (6),

we can write the water saturation equation as:

$$\phi\frac{\partial S_w}{\partial t} + \nabla \cdot [\mathbf{u}_t f(S_w)] = -\tilde{q}_w. \tag{9}$$

The corresponding pressure equation can be formed by introducing the expression for $\mathbf{u}_t$ (Eq. (8) into Eq. (7)):

$$\nabla \cdot (\mathbf{k}\lambda_t(S_w) \cdot \nabla p) = \tilde{q}_t, \tag{10}$$

where we have introduced the total mobility λ_t, defined via:

$$\lambda_t = \lambda_w + \lambda_o = \frac{k_{rw}}{\mu_w} + \frac{k_{ro}}{\mu_o}. \tag{11}$$

The pressure and saturation equations describe the flow of two immiscible fluids. The pressure equation (10) is very similar to the single-phase pressure equation (4) except the λ_t term replaces $1/\mu$. The single-phase limit is recovered if the two phases have identical properties and do not interfere. For such a system, $k_{rw} = S_w$, $k_{ro} = S_o = 1 - S_w$, and $\mu_w = \mu_o$, giving $\lambda_t = 1/\mu_w = 1/\mu_o$ and $f(S_w) = S_w$ (in Eq. (9)). In this case, the system is of unit mobility ratio.

More general models for two-phase flow include the effects of compressibility, gravity and capillary pressure. The representation of the system in terms of pressure and saturation equations is still possible; see Peaceman [69] and Aziz and Settari [6] for details.

Many of the upscaling techniques described below compute upscaled transmissibility rather than permeability. Transmissibility is an interblock (numerical) quantity defined at cell interfaces that relates the flow from one block to an adjacent block in terms of the pressure difference between the blocks; i.e., $q_{i+1/2} = (T_x)_{i+1/2}(p_i - p_{i+1})$, where q is flow rate, T_x is transmissibility in the x direction and subscripts designate grid block (i or $i+1$) or interface ($i+1/2$). The transmissibility in x between grid blocks i and $i+1$ is given by:

$$(T_x)_{i+1/2} = \frac{2(k_x)_{i+1/2}\Delta y \Delta z}{\Delta x_{i+1} + \Delta x_i}, \tag{12}$$

where Δx, Δy and Δz are grid block sizes and $(k_x)_{i+1/2}$ is the weighted harmonic average of the x component of permeability in blocks i and $i+1$:

$$(k_x)_{i+1/2} = \frac{(\Delta x_i + \Delta x_{i+1})(k_x)_i(k_x)_{i+1}}{\Delta x_{i+1}(k_x)_i + \Delta x_i(k_x)_{i+1}}. \tag{13}$$

Transmissibilities and interface permeabilities in the y and z directions are analogous. The formulation above is for the case of a two-point flux approximation. Multipoint flux approximations are significantly more complex; see [2, 35, 59] for details.

2.3   Classifications of upscaling procedures

There are several different ways in which upscaling techniques can be classified. Here we will classify the various methods in terms of the types of parameters that are upscaled (single or two-phase flow parameters) and the way in which these parameters are computed (e.g., using local or global calculations). We first consider classification by the types of parameters that are upscaled.

For single-phase flow involving a single component, the only parameters to be upscaled are porosity and the absolute permeability or transmissibility. In the more general case of two-phase flow, the absolute permeability (or transmissibility) and porosity as well as the relative permeability can be upscaled. However, in many cases it is possible to develop reasonably accurate coarse scale models for two-phase flow with only the absolute permeability or transmissibility and porosity upscaled, particularly when accurate upscaling is used in conjunction with flow-based grid generation. In models of this type, the geocellular scale relative permeabilities are used directly on the coarse scale. Thus, even for two (or three) phase flow systems, we can still generate coarse scale models with only absolute permeability or transmissibility and porosity upscaled in some cases. We refer to this type of approach as "single-phase parameter upscaling" or "single-phase upscaling," with the understanding that it can be used for both single and two-phase (or multiphase) flow problems. Such approaches can be further classified as permeability or transmissibility upscaling procedures.

In other cases, the two-phase flow parameters (e.g., k_{rj} and p_c) are also upscaled. We refer to this type of approach as a "two-phase parameter upscaling" or simply "two-phase upscaling." Another way to view this classification is in terms of the governing pressure and saturation equations. In single-phase upscaling, the pressure equation is modified but the saturation equation appears essentially the same (though ϕ is upscaled). In two-phase upscaling, by contrast, parameters in both equations are modified.

The second type of classification is related to the way in which upscaled parameters (single or two-phase) are computed. In all cases the intent of the upscaling procedure is to replace the fine model with a coarse model. In a purely local procedure, coarse scale parameters are computed by considering only the fine scale region corresponding to the target coarse block. No additional fine scale information is included in the upscaling calculation. In a global upscaling technique, the entire fine scale model is simulated for the calculation of the coarse scale parameters. The assumption here is that the coarse scale parameters will be applicable to other (related) flow scenarios.

There are several important variants of the purely local and global approaches. Of interest to us will be "extended local" and "quasi global" upscaling techniques. In extended local procedures, coarse scale parameters are computed by considering the

region corresponding to the target coarse block plus a fine scale "border region" or skin around this region. Coarse scale quantities are generally computed by averaging the fine scale solution (e.g., pressure and velocity) only over the region corresponding to the target coarse block. In quasi global methods, global flow data informs the upscaling technique but this information is only approximate. For example, in the case of a quasi global two-phase parameter upscaling, the global flow field might be estimated from a single solution of the single-phase pressure equation rather than by a more computationally expensive transient solution of the two-phase flow equations. We will discuss local, extended local, global and quasi global upscaling techniques later in this review.

The single-phase upscaling procedures described here all require some amount of computation, and this represents an overhead for the reservoir simulation. The time required for most of the methods is, however, very small compared to the cost of the fine scale multiphase flow simulation (it is usually also small compared to the cost of the coarse scale multiphase simulation). For further discussion of these timing issues, see [87, 16].

2.4 Multiscale methods

Another important class of upscaling procedures are multiscale finite element and finite volume approaches. Within the context of reservoir simulation, for example, Hou and Wu [49] and Arbogast and Bryant [4] developed finite element based approaches, while Jenny *et al.* [50] developed an approach based on a full tensor flux-continuous finite volume procedure. These methods have the benefit that the fine scale permeability information enters into the global solution in a systematic way. To date, these procedures have mainly been applied to the pressure equation; transport calculations have generally been performed by reconstructing the fine scale velocity field. This reconstruction, which can also be accomplished using other procedures (see, e.g., [77, 43, 39, 16]), entails the use of the fine grid for the solution of the saturation equation.

Dual grid approaches (e.g., [77, 43, 39]) are also related to multiscale methods. In these procedures, different grids are defined and reconstruction techniques are applied to determine fine scale variables from the global coarse scale solution. These methods can provide accurate results in many cases, though they, like multiscale procedures, require that the fine scale permeability information be stored and used during the global solution. For a more detailed discussion of multiscale methods and their relationship to upscaling procedures, see [40].

3 Coarse scale pressure equation and analytical upscaling methods

We now consider the upscaling of absolute permeability. As indicated above, even for many two-phase flow problems, particularly when the overall level of coarsening is not excessive (e.g., 1-2 order of magnitude reduction in the total number of cells for a typical problem), this has been found to be a reasonable approach. Some theoretical justification for neglecting the upscaling of relative permeability, in the context of moderately coarsened models and flow-based grids, is offered by Durlofsky [27]. As the degree of coarsening becomes very high, however, upscaled two-phase flow functions will generally be required.

3.1 Fine and coarse scale pressure equations

For now we consider steady, single-phase incompressible flow with no source terms (Eq. (4) with $\tilde{q} = 0$). We introduce a conceptual two-scale model for permeability; i.e., permeability varies on two distinct scales referred to as $\mathbf{x}$ and $\mathbf{y}$. The $\mathbf{x}$ scale is a slow scale, meaning that variations in $\mathbf{x}$ are relatively gradual. The $\mathbf{y}$ scale, by contrast, is a fast scale, and captures the fine scale variation of permeability. With this $\mathbf{k}(\mathbf{x}, \mathbf{y})$ representation, the dimensionless pressure equation is written as follows:

$$\nabla \cdot (\mathbf{k}(\mathbf{x}, \mathbf{y}) \cdot \nabla p) = 0. \tag{14}$$

Eq. (14) is the pressure equation with the permeability field fully resolved. Homogenization procedures, as applied by Bourgeat [10] and Saez *et al.* [81], among others, allow Eq. (14) to be replaced with an analogous equation in which variations need only be resolved on the $\mathbf{x}$ (slow) scale. The pressure equation in this case can be written as:

$$\nabla \cdot (\mathbf{k}^*(\mathbf{x}) \cdot \nabla p^c) = 0, \tag{15}$$

where $\mathbf{k}^*$ is referred to as the effective permeability tensor and p^c is the coarse scale pressure. Note that $\mathbf{k}^*$ is defined on the scale of $\mathbf{x}$; $\mathbf{y}$-scale variations, which exist in $\mathbf{k}$, have been homogenized or averaged. This means that, in solving Eq. (15), we need not resolve effects on the scale of $\mathbf{y}$, which leads to significant computational savings.

The upscaling of $\mathbf{k}(\mathbf{x}, \mathbf{y})$ to $\mathbf{k}^*(\mathbf{x})$, and the replacement of Eq. (14) by Eq. (15), is mathematically valid only in certain circumstances [10, 81]. Specifically, the region over which $\mathbf{k}^*$ is computed must be large relative to the fast ($\mathbf{y}$) scale of variation (e.g., the correlation length of the heterogeneity field). In addition, Eq. (15) is technically not applicable near boundaries or sources. However, even though there is often not a clear theoretical justification for replacing Eq. (14) by Eq. (15), there is a large body of numerical evidence justifying this procedure. The coarse scale

permeability in these more general cases is properly referred to as the equivalent grid block permeability tensor rather than an effective permeability. See Durlofsky [26] for more discussion of this point. A wide variety of techniques for computing these grid block permeabilities is available, as we shall discuss.

3.2 Power averaging procedures

The simplest techniques for computing grid block permeabilities are power averaging procedures, introduced by Deutsch [21] (see also discussion in Wen and Gómez-Hernández [90]). These approaches do not require any numerical solutions so they are very efficient computationally. The basic approach entails computing upscaled permeability components, here designated k_i^*, via:

$$k_i^* = \left(\frac{1}{V_b} \int_{V_b} [k_i(\mathbf{y})]^{\omega_i} \; dV \right)^{1/\omega_i},$$ (16)

where V_b is the coarse block bulk volume and both the fine scale permeability $\mathbf{k}(\mathbf{y})$ and the upscaled permeability $\mathbf{k}^*$ are considered to be diagonal tensors, with i designating a diagonal component. The power averaging exponent ω_i can vary with direction i. This type of averaging procedure can be readily applied to coarse grid cells of any shape, so it is suitable for use with irregular grids.

The power averaging exponent ω_i is constrained to lie between -1 and 1. The extremes correspond to layered systems: for flow parallel to the layers $\omega = 1$ (arithmetic average), while for flow perpendicular to the layers $\omega = -1$ (harmonic average). The geometric mean corresponds to the limit $\omega \to 0$. In this case, Eq. (16) becomes:

$$k_i^* = \exp \left(\frac{1}{V_b} \int_{V_b} \log [k_i(\mathbf{y})] \; dV \right).$$ (17)

Power averaging can also be applied using a combination of two different values of ω. For example, for a structured, approximately layered system in the $x - z$ coordinate system, k_x^* might be computed by harmonically averaging along each layer in x and then arithmetically averaging these layer averages. The use of this type of procedure provides power averaging approaches with a higher degree of applicability. Power averaging exponents may be determined in practice by tuning against numerical upscaling results. The assumption then is that the same ω_i can be used for models with similar permeability distributions.

The fact that ω_i can vary with direction leads to the general observation that the upscaled permeability can be anisotropic even when the underlying permeability field $k(\mathbf{y})$ is everywhere isotropic. For the power averaging approach described here, the upscaled permeability is still a diagonal tensor. However, for the more general numerical methods described below, the upscaled permeability is typically a full tensor quantity.

Other analytical procedures for permeability upscaling include the renormalization approach of King [55] and the full tensor averaging technique of Kasap and Lake [52]. Both of these approaches are very efficient and have been shown to perform well for some classes of problems. Like power averaging techniques, however, they lack the generality of the numerical procedures described below.

3.3 Upscaling of porosity

Porosity on the coarse scale, designated ϕ^*, is computed such that pore volume is exactly conserved between the fine and coarse scales. Specifically, ϕ^* is computed via:

$$\phi^* = \frac{1}{V_b} \int_{V_b} \phi(\mathbf{y}) \, dV, \tag{18}$$

where V_b again designates bulk volume.

4 Purely local and extended local numerical procedures to compute $\mathbf{k}^*$ and T^*

The more robust and accurate procedures for computing $\mathbf{k}^*$ and T^* require the solution of the fine scale pressure equation over the target coarse region. As discussed below, in some cases it is beneficial to use an extended local approach in order to include the effects of neighboring regions in these calculations. Global and quasi global procedures can also be applied, as described in §5. We now consider a variety of approaches, beginning with the simplest purely local techniques. Much of the description below is for two-dimensional systems. The three-dimensional procedures have, in most cases, also been implemented and are typically straightforward generalizations of the two-dimensional methods.

Different upscaling techniques force agreement in different quantities. For example, Zijl and Trykozko [94] describe approaches for computing upscaled permeabilities using pressure-flux averaging, pressure-dissipation averaging, or flux-dissipation averaging. The relative advantages and disadvantages of the various approaches are also discussed. When periodic boundary conditions are applied (discussed below), the upscaled permeability is the same in all cases. In the discussion here we do not consider all of these approaches for upscaling but focus instead on the use of pressure and velocity (or flux) averaging. It is possible that alternate procedures may provide improved results in some cases.

In all of the procedures described below, finite volume (often referred to as finite difference) methods are applied for the numerical solutions. If the fine scale permeability is a diagonal tensor and the grid is orthogonal, the standard two-point flux approximation (using harmonic averages of the appropriate permeability

component, as in Eq. (13)) can be used. In this case a five point finite difference stencil is obtained in two dimensions and a seven point stencil in three dimensions. In cases in which permeability is a full tensor and/or the grid is nonorthogonal, multipoint flux techniques, as described in [2, 35, 59], are technically required. In some cases, however, the error from using a two-point flux approximation for such systems may be small. This will be illustrated in some of the examples below.

4.1   Fixed pressure boundary conditions

In computing equivalent grid block permeabilities or transmissibilities, we solve Eq. (14) over the fine scale region corresponding to the target coarse block or interface. A significant issue in any local or extended local upscaling technique is the choice of boundary conditions to be imposed. Because the actual conditions imposed on the region during the course of a flow simulation are not known a priori and will in general vary, there is always some ambiguity in specifying the boundary conditions in the upscaling procedure. There is additionally some freedom in how the upscaled $\mathbf{k}^*$ or T^* is computed from the local fine grid solution. We now discuss these issues in turn.

Upscaling methodologies will first be discussed within the context of a structured, rectangular grid. The extension of these approaches to more general control volumes will then be described. Consider the rectangular domain illustrated in Fig. 1. This domain corresponds to a single coarse grid block. The fine grid permeability field (on the $\mathbf{y}$-scale) is not shown. Our intent is to solve Eq. (14) over this domain and then use this solution to compute the equivalent grid block permeability tensor. Permeability upscaling is considered first. We discuss the boundary conditions for this problem and then describe how to compute $\mathbf{k}^*$ from the fine grid solution.

The simplest and in many ways the most intuitive boundary conditions for this problem might be a constant pressure - no flow boundary specification. For the system shown in Fig. 1, these boundary conditions require us to solve Eq. (14) twice. In the first solution we set

$$p(0, y_2) = 1, \tag{19a}$$
$$p(L_1, y_2) = 0, \tag{19b}$$
$$\mathbf{u}(y_1, 0) \cdot \mathbf{n}_1 = \mathbf{u}(y_1, L_2) \cdot \mathbf{n}_2 = 0, \tag{19c}$$

while in the second solution the pressure difference is specified to be in the y_2 direction. From these two solutions we can compute total flow rates through the faces of the region; i.e., from the first solution:

$$q_1 = \Delta y_3 \int_0^{L_2} \mathbf{u}(L_1, y_2) \cdot \mathbf{n}_4 \; dy_2 = \sum_{l=1}^{N_f} (\mathbf{u}_l \cdot \mathbf{n}_4) \, A_l, \tag{20}$$
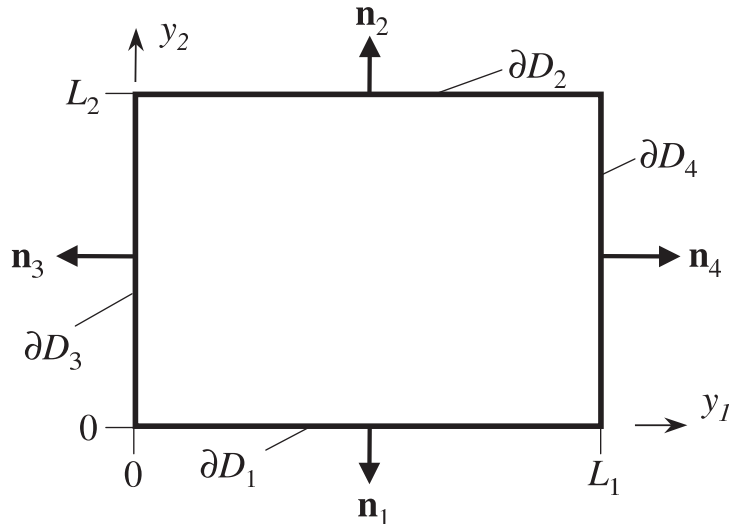
11

Figure 1: Schematic of rectangular local solution domain.

where the sum is over cells on edge ∂D_4 (Fig. 1), N_f is the number of fine cells in the y_2 direction and $A_l = (\Delta y_2)_l \Delta y_3$, where Δy_3 is the (constant) thickness in the third dimension. Similarly, q_2 can be computed from the second solution. Then, the upscaled permeability can be computed by equating the total flow rate from the local fine scale solution with the flow rate that would result for a homogeneous region of permeability k_1^* subject to the same boundary conditions. This gives:

$$k_1^* = \frac{q_1 L_1}{L_2 \Delta y_3 \Delta p},$$ (21)

where $\Delta p = 1$ from Eqs. (19). The quantity k_2^* is computed in a similar manner.

In many cases, the k_1^* and k_2^* computed in this way provide reasonably accurate coarse block permeabilities. However, the boundary conditions and method for computing $\mathbf{k}^*$ from the local fine grid solution in this case preclude the calculation of the cross terms of $\mathbf{k}^*$. These terms can be significant in cases where the grid is not locally K-orthogonal (by K-orthogonality we mean that the grid geometry and permeability can be represented in terms of two-point fluxes in the finite volume discretization). Therefore, procedures for computing a full tensor $\mathbf{k}^*$ are required for some cases.

One approach for generating full tensor coarse block permeabilities is to post-process the fine grid solution in a manner different to that used in Eqs. (20) and (21). Because the no flow boundary conditions do not permit the calculation of a full tensor $\mathbf{k}^*$ via integration over boundaries, we instead compute volume averaged velocities and pressure gradients over the entire flow domain (e.g., [80, 93]).

Specifically, we compute

$$\langle \mathbf{u} \rangle^j = \frac{1}{V_b} \int_V \mathbf{u}^j \ dV = \frac{1}{V_b} \sum_{l=1}^{N_t} \mathbf{u}_l V_l, \tag{22a}$$

$$\langle \nabla p \rangle^j = \frac{1}{V_b} \int_V (\nabla p)^j \ dV = \frac{1}{V_b} \sum_{l=1}^{N_t} (\nabla p)_l V_l, \tag{22b}$$

where $j = 1, 2$ indicates the flow solution (i.e., $j = 1$ denotes the solution with the pressure difference in the y_1 direction; $j = 2$ the solution with the pressure difference in the y_2 direction) and the sums are over all N_t fine blocks comprising the target region (V_l designates the bulk volume of fine scale cell l). Because both $\langle \mathbf{u} \rangle$ and $\langle \nabla p \rangle$ have two components (for a two-dimensional problem), and because we solve two flow problems, four components of $\mathbf{k}^*$ can be calculated from these two flow solutions. Specifically, we can write:

$$\langle u \rangle_1^1 = -(k_{11}^* \langle \nabla p \rangle_1^1 + k_{12}^* \langle \nabla p \rangle_2^1), \tag{23a}$$
$$\langle u \rangle_2^1 = -(k_{21}^* \langle \nabla p \rangle_1^1 + k_{22}^* \langle \nabla p \rangle_2^1), \tag{23b}$$
$$\langle u \rangle_1^2 = -(k_{11}^* \langle \nabla p \rangle_1^2 + k_{12}^* \langle \nabla p \rangle_2^2), \tag{23c}$$
$$\langle u \rangle_2^2 = -(k_{21}^* \langle \nabla p \rangle_1^2 + k_{22}^* \langle \nabla p \rangle_2^2), \tag{23d}$$

where the subscript on $\langle u \rangle$ and $\langle \nabla p \rangle$ designates the vector component and the superscript the flow problem. This set of equations can be rearranged to give a matrix equation:

$$
\begin{pmatrix}
\langle \nabla p \rangle_1^1 & \langle \nabla p \rangle_2^1 & 0 & 0 \\
0 & 0 & \langle \nabla p \rangle_1^1 & \langle \nabla p \rangle_2^1 \\
\langle \nabla p \rangle_1^2 & \langle \nabla p \rangle_2^2 & 0 & 0 \\
0 & 0 & \langle \nabla p \rangle_1^2 & \langle \nabla p \rangle_2^2
\end{pmatrix}
\begin{pmatrix}
k_{11}^* \\
k_{12}^* \\
k_{21}^* \\
k_{22}^*
\end{pmatrix}
= -
\begin{pmatrix}
\langle u \rangle_1^1 \\
\langle u \rangle_2^1 \\
\langle u \rangle_1^2 \\
\langle u \rangle_2^2
\end{pmatrix},
\tag{24}
$$

which can now be solved to determine the components of $\mathbf{k}^*$.

With the boundary conditions described by Eqs. (19), the $\mathbf{k}^*$ computed via Eq. (24) will not in general be symmetric. Various procedures can be applied to enforce symmetry; the simplest approach is to set each of the cross terms equal to $(k_{12}^* + k_{21}^*)/2$. A better approach to ensure symmetry is to solve a least square problem rather than Eq. (24). In this case we enforce symmetry by adding an equation of the form $k_{12}^* - k_{21}^* = 0$. The resulting set of equations is now given by:

$$
\begin{pmatrix}
\langle \nabla p \rangle_1^1 & \langle \nabla p \rangle_2^1 & 0 & 0 \\
0 & 0 & \langle \nabla p \rangle_1^1 & \langle \nabla p \rangle_2^1 \\
\langle \nabla p \rangle_1^2 & \langle \nabla p \rangle_2^2 & 0 & 0 \\
0 & 0 & \langle \nabla p \rangle_1^2 & \langle \nabla p \rangle_2^2 \\
0 & 1 & -1 & 0
\end{pmatrix}
\begin{pmatrix}
k_{11}^* \\
k_{12}^* \\
k_{21}^* \\
k_{22}^*
\end{pmatrix}
= -
\begin{pmatrix}
\langle u \rangle_1^1 \\
\langle u \rangle_2^1 \\
\langle u \rangle_1^2 \\
\langle u \rangle_2^2 \\
0
\end{pmatrix}.
\tag{25}
$$

The last equation can be rescaled if necessary so these matrix elements are of the same magnitude as the other terms.

In addition to symmetry, we also require that $\mathbf{k}^*$ be positive definite (i.e., have positive eigenvalues). In two dimensions this requires that $k_{11}^* > 0$, $k_{22}^* > 0$ and $k_{11}^* k_{22}^* > (k_{12}^*)^2$. This requirement is generally satisfied by the methods described here. In the few cases when this is not satisfied, $\mathbf{k}^*$ can be recomputed using outlet averaging (in which case k_{12}^* is undetermined) or using periodic boundary conditions (described below).

The pressure - no flow boundary conditions just discussed are not the most general boundary conditions that can be used. Another alternative is to use boundary conditions that specify a linear pressure variation along the sides parallel to the direction of the pressure gradient (e.g., King $et\ al.$ [53, 54]). Then, rather than the boundary conditions of Eqs. (19), the boundary conditions for the first flow problem are:

$$p(0, y_2) = 1, \tag{26a}$$

$$p(L_1, y_2) = 0, \tag{26b}$$

$$p(y_1, 0) = p(y_1, L_2) = 1 - y_1/L_1. \tag{26c}$$

Unlike the pressure - no flow specification, these boundary conditions do allow for flow out of the domain in a direction transverse to the pressure difference. Thus, a full tensor $\mathbf{k}^*$ can be computed from the integrated flow rates through the boundaries. For example, from the solution of Eq. (14) subject to Eqs. (26), we can compute

$$q_1^1 = \Delta y_3 \int_0^{L_2} \mathbf{u}^1(L_1, y_2) \cdot \mathbf{n}_4 \, dy_2, \quad q_2^1 = \Delta y_3 \int_0^{L_1} \mathbf{u}^1(y_1, L_2) \cdot \mathbf{n}_2 \, dy_1. \tag{27}$$

Then,

$$k_{11}^* = \frac{q_1^1 L_1}{L_2 \Delta y_3 \Delta p}, \quad k_{21}^* = \frac{q_2^1}{\Delta y_3 \Delta p}, \tag{28}$$

where again $\Delta p = 1$ in this case. The other two components of $\mathbf{k}^*$ can be computed from the second solution (pressure difference in y_2 direction). The tensor computed in this manner will again not be symmetric in general.

The solution using linear pressure boundary conditions can also be used to compute $\mathbf{k}^*$ within the volume averaging context described via Eqs. (22) to (25). The $\mathbf{k}^*$ thus computed will in general differ from the $\mathbf{k}^*$ computed via Eqs. (27) and (28). It is not clear from previous work which of these approaches is the more accurate – it is likely that the method of choice will be case dependent.

4.2 Periodic boundary conditions

We next describe the use of periodic boundary conditions for the calculation of $\mathbf{k}^*$. This boundary specification eliminates some of the ambiguity of the other methods in that it provides the same result for either method of post-processing of the fine grid solution. Periodic boundary conditions have been applied and analyzed by a number of investigators including Durlofsky [26], Boe [9], Pickup *et al.* [72] and Wen *et al.* [89, 88]. These boundary conditions again require that two local fine scale problems be solved. The specific form of the boundary conditions derives from the assumption that the system is replicated periodically in space and that the global pressure (on the scale of $\mathbf{x}$) can be approximated as $p = p_0 + \mathbf{G} \cdot (\mathbf{x} - \mathbf{x}_0)$, where $\mathbf{G} = G_1 \mathbf{i}_1 + G_2 \mathbf{i}_2$ is a constant vector. These are both reasonable approximations in many cases, though inaccuracy can result when the assumption of periodicity disrupts larger scale permeability connectivity.

With reference to Fig. 1, periodic boundary conditions can be specified via:

$$p(y_1, 0) = p(y_1, L_2) - G_2 L_2 \qquad \text{on } \partial D_1 \text{ and } \partial D_2, \qquad (29\text{a})$$
$$p(0, y_2) = p(L_1, y_2) - G_1 L_1 \qquad \text{on } \partial D_3 \text{ and } \partial D_4, \qquad (29\text{b})$$
$$\mathbf{u}(y_1, 0) \cdot \mathbf{n}_1 = -\mathbf{u}(y_1, L_2) \cdot \mathbf{n}_2 \qquad \text{on } \partial D_1 \text{ and } \partial D_2, \qquad (29\text{c})$$
$$\mathbf{u}(0, y_2) \cdot \mathbf{n}_3 = -\mathbf{u}(L_1, y_2) \cdot \mathbf{n}_4 \qquad \text{on } \partial D_3 \text{ and } \partial D_4. \qquad (29\text{d})$$

By selecting two linearly independent pairs of (G_1, G_2), and by solving Eq. (14) subject to Eqs. (29), we can compute $\mathbf{k}^*$ using either Eqs. (22) to (24) or Eqs. (27) and (28), with identical results. In practice, in the first problem we set $G_1 = 1$ and $G_2 = 0$ and in the second problem $G_1 = 0$ and $G_2 = 1$.

Periodic boundary conditions have several useful features. They guarantee that the resulting $\mathbf{k}^*$ will be symmetric and positive definite. Thus, no post-processing of the result is necessary to ensure that these two criteria are met. In a study comparing the use of several different boundary conditions for the calculation of $\mathbf{k}^*$, Pickup *et al.* [72] demonstrated that periodic boundary conditions performed reliably in the example problems considered. However, they did demonstrate that in many cases the differences between the various methods were slight.

4.3 Transmissibility upscaling

In the descriptions above, we considered boundary specifications and averaging procedures for the calculation of upscaled permeability tensors. These approaches can also be applied to the direct calculation of upscaled transmissibility. This provides more accurate coarse scale models in many cases because it eliminates the additional approximations that result when transmissibility is calculated from the grid block $\mathbf{k}^*$ (via the weighted harmonic averaging indicated in Eq. (13)). Illustrations and

discussion of the enhanced accuracy of transmissibility upscaling in some cases can be found in [79, 3, 16].

We consider a two-dimensional system in the $y_1 - y_2$ plane (of thickness Δy_3) with permeability everywhere diagonal ($k_{12} = k_{21} = 0$). Directional permeabilities will be referred to as k_1 and k_2. The purely local problem, shown in Fig. 2, now includes the fine scale region corresponding to the two coarse blocks (designated i and $i + 1$) that share the target interface $i + 1/2$ (indicated in bold in Fig. 2). Note that it is possible to use an even smaller region, containing only the two half-cells on either side of the target interface. Any of the boundary conditions discussed above can be applied to the local problem illustrated in Fig. 2. Following the solution of the fine scale pressure equation subject to these boundary conditions, we compute the average pressure over the region corresponding to coarse block i

$$\langle p \rangle_i = \frac{1}{V_b} \sum_{l=1}^{N_t} p_l V_l, \tag{30}$$

where all quantities are as defined earlier. A similar expression gives $\langle p \rangle_{i+1}$. The flow rate across the interface, designated $(q_1)_{i+1/2}$, is given by:

$$(q_1)_{i+1/2} = \sum_{l=1}^{N_f} \left(\mathbf{u}_l \cdot \mathbf{n} \right) A_l, \tag{31}$$

where N_f is the number of fine cells along the interface $i + 1/2$. From these quantities, the upscaled transmissibility in the y_1 direction (T_1^*) can be computed via:

$$(T_1^*)_{i+1/2} = \frac{(q_1)_{i+1/2}}{\langle p \rangle_i - \langle p \rangle_{i+1}}, \tag{32}$$

For the calculation of T_2^*, a local problem centered on the interface with normal $\mathbf{i}_2$ is solved. An expression similar to Eq. (32) provides T_2^*. The T^* computed as described here are applicable for a two-point flux approximation. If full-tensor effects or grid nonorthogonality are important, a multipoint flux approximation may be required. In this case transmissibility upscaling could be extended to a multipoint flux context through use of an approach along the lines of that developed by Jenny *et al.* [50].

4.4   Extended local procedures: use of border regions

It has been observed by a number of authors that improved accuracy in $\mathbf{k}^*$ and T^* can be achieved if a larger local problem is solved (see, e.g., Gómez-Hernández and Journel [42]; Holden and Lia [46]; Hou and Wu [49]; Wu *et al.* [93]; Wen *et al.* [89, 87, 88]). By including neighboring regions in the calculation of $\mathbf{k}^*$ or T^* for a particular coarse block or interface, the effects of large scale permeability
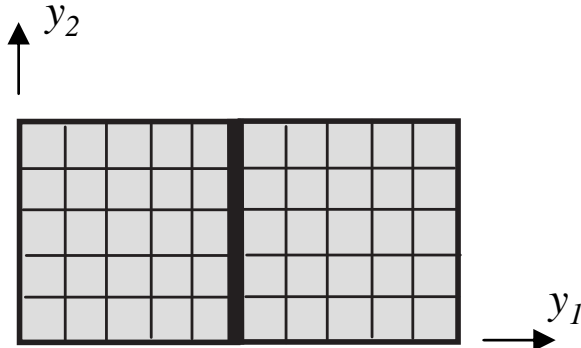
Figure 2: Schematic of local solution domain for transmissibility upscaling.

connectivity (or lack of connectivity) can be better captured, particularly when the permeability field contains features that are not oriented with the grid. A "border region," containing the fine scale permeability field corresponding to a single ring of coarse blocks around the target coarse block, is shown in Fig. 3. In the figure, the finer lines represent the fine grid, the heavier lines the coarse grid, and the shaded block is the target cell for which $\mathbf{k}^*$ is to be computed. We quantify the size of the extended local region via the parameter r, which defines the number of rings of coarse cells that comprise the border region (extended local solutions include all of the fine cells corresponding to the target cell plus border regions). The region shown in Fig. 3, which corresponds to $r = 1$, is appropriate for permeability upscaling; the extended local region would be centered around the target interface in the case of transmissibility upscaling. Any of the boundary conditions discussed above can now be applied on the expanded domain shown in the figure.

For the computation of $\mathbf{k}^*$, because we now wish to compute the upscaled quantity for only a portion of the fine scale domain over which Eq. (14) is solved (the target coarse block), we apply the volume averaging procedure described above rather than the integration over boundaries. Specifically, using Eqs. (22), we compute $\langle \mathbf{u} \rangle$ and $\langle \nabla p \rangle$ over the shaded region in Fig. 3 and then apply Eq. (24) or (25) to form $\mathbf{k}^*$. We note that, even if periodic boundary conditions are applied, the $\mathbf{k}^*$ computed using Eq. (24) will not in general be symmetric. This is because the symmetry provided by periodic boundary conditions for purely local upscaling is lost when border regions are applied. Symmetry can be approximately recovered through use of the least square technique (Eq. (25)). For the case of transmissibility upscaling, the averaging is performed as described above for the purely local problem (again only over the target cells and interface).

It is reasonable to expect that the effect of the boundary specification on the computed $\mathbf{k}^*$ or T^* will be less when border regions are used and that results using
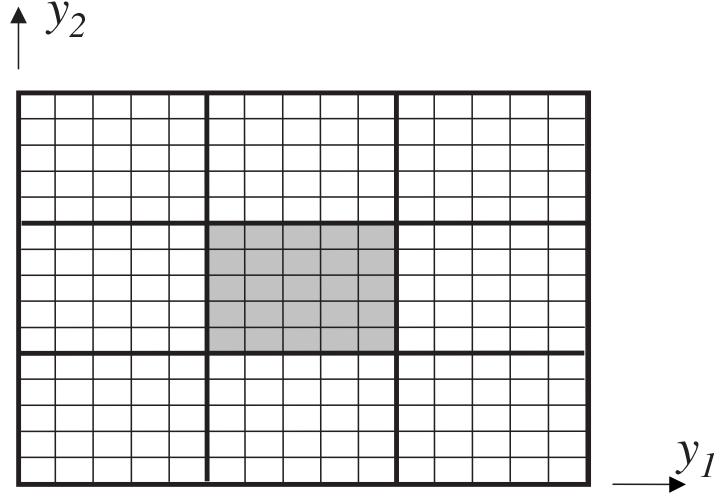
Figure 3: Fine and coarse grids with border region (target cell in center).

different boundary conditions will tend to converge. In limited tests, some of which we will describe below, this did in fact appear to be the case [88]. We note additionally that, again in limited tests, the use of one bordering ring surrounding the target cell ($r = 1$) appears to suffice. Relatively little improvement was observed when a two-ring region was applied [89, 88].

4.5   Irregular coarse grid control volumes

Up to this point, we have considered upscaling procedures applicable for structured grids comprised of rectangular blocks. The procedures described can readily be extended to three dimensions, so they are equally applicable to brick-shaped control volumes. We now discuss the generalization of these approaches to irregular control volumes.

We assume for the present discussion that the underlying geocellular grid is structured and is comprised of rectangular cells. In general, the irregular coarse scale cell will not be "aligned" with respect to the fine grid. By this we mean that the vertices of the coarse cell will not coincide with the corner points of the fine geocellular grid. This case is illustrated in Fig. 4. Nine coarse blocks are shown in the figure, as is the underlying fine grid. The central coarse cell is the target coarse cell; i.e., the one for which we wish to compute $\mathbf{k}^*$. Techniques for upscaling with general quadrilaterals when the fine and coarse grids are aligned were developed by Edwards [32] and Eek-Jensen *et al.* [36].

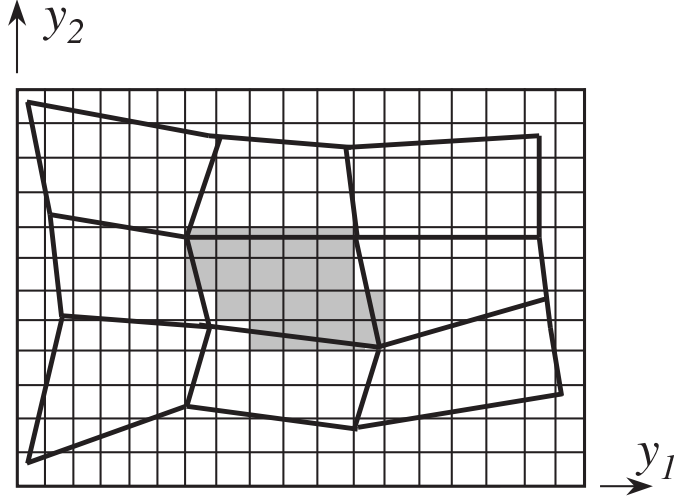The border region approach described above lends itself quite naturally to this

Figure 4: Non-aligned fine and coarse grids with border region ($r = 1$).

calculation. We define the local solution domain as the rectangular region containing the coarse cell corner points plus a number of additional fine grid cells corresponding to the dimensions of the target coarse cell. For example, for the case where the coarse cell corner points fall within a 6×4 rectangle of fine cells (as in Fig. 4), the local problem will be expanded by 6 cells in the $-y_1$ and $+y_1$ directions and by 4 cells in the $-y_2$ and $+y_2$ directions. In this case, the local solution will contain 18×12 fine cells (the entire domain shown in Fig. 4).

In the case of a triangular or polygonal coarse scale control volume, the local solution domain could be defined to include all fine scale blocks whose centroids fall within a prescribed distance of the centroid of the target cell. This distance could be specified in terms of a typical linear dimension of the target cell. Thus, regardless of the shape of the coarse cell, a rectangular domain containing fine scale cells corresponding to the neighbors of the target cell can be established.

We then solve Eq. (14) subject to boundary conditions to determine the fine scale solution over the domain of Fig. 4. Following the solution of the local fine scale problem, we compute $\langle \mathbf{u} \rangle$ and $\langle \nabla p \rangle$ over the coarse cell region and then apply Eq. (24) or (25) to form $\mathbf{k}^*$. Some care is needed in computing these averages since the fine and coarse grids are not aligned.

The simplest approach is to include in the averaging only those fine cells whose centers fall within the boundaries of the coarse cell. This approach is illustrated in Fig. 4, where the fine blocks indicated by shading (the blocks falling within the coarse cell) are the cells contributing to the calculation of $\langle \mathbf{u} \rangle$ and $\langle \nabla p \rangle$. Another approach, which might offer better accuracy in some cases, would be to apply an area weighting using all fine scale blocks that have some portion of their area within

the coarse cell. For transmissibility upscaling (within a two-point flux context), we apply Eqs. (30)-(32) to determine T^*. The summation in Eq. (30) is again only over the cells whose centers fall within the target cell. The flux calculation accounts for the fact that the fine grid and the coarse grid interface are non-aligned through the $\mathbf{u}_l \cdot \mathbf{n}$ term in Eq. (31). This approach for computing T^* will in general incur some error in cases when the system is not K-orthogonal.

In a number of test cases, the procedure described above was shown to provide coarse scale flow results of reasonable accuracy (Wen *et al.* [87]). However, it is possible that an improved treatment of the coarse cell geometry may be required for some types of problems. This can be accomplished through use of a triangle based finite element method for the solution of the local fine grid problem. Such an approach was developed by He *et al.* [45], in which a non-conforming finite element method (which is very similar to a mixed finite element method for this problem) was applied. This enables the detailed resolution of grid block boundaries and fine scale permeability variation as well as the accurate solution of the governing pressure equation. See [45, 44, 25] for further description and illustrations of the performance of this approach.

4.6 Upscaling in the near-well region

The basic assumption in all of the local and extended local procedures considered above is that the flow can be described locally as essentially linear; i.e., the large scale pressure gradient ∇p is approximately constant over the target region. This assumption is not applicable in the near-well region, as the steady state pressure in the vicinity of a well away from boundaries varies as $\log r$, where r is radial distance. We now describe an approach for near-well upscaling which can be classified as an extended local technique, though the local problem is driven by a well rather than by a large scale linear pressure field.

Wells are represented in reservoir simulators through use of a well index, here designated by W_i, which relates the wellbore pressure in block i (p_i^w) to the grid block pressure p_i and well flow rate q_i^w via:

$$q_i^w = W_i(p_i - p_i^w), \tag{33}$$

in dimensionless terms. In an (x, y, z) coordinate system, the default well index W_i^d for a fully penetrating vertical well in block i is given by the Peaceman expression [70]:

$$W_i^d = \left(\frac{2\pi \sqrt{k_x k_y} \, \Delta z}{\log \frac{r_w}{r_o}} \right)_i, \tag{34}$$

20

where

$$r_0 = 0.28 \frac{\sqrt{\sqrt{\frac{k_y}{k_x}}\Delta x^2 + \sqrt{\frac{k_x}{k_y}}\Delta y^2}}{\sqrt[4]{\frac{k_y}{k_x}} + \sqrt[4]{\frac{k_x}{k_y}}}. \tag{35}$$

Here permeability is again assumed to be diagonal. Expressions similar to Eqs. (34) and (35) are used for horizontal or deviated wells.

If no near-well upscaling is applied, the well index can be computed using Eqs. (34)-(35), but with the upscaled permeability components k_x^* and k_y^* replacing k_x and k_y. We refer to this well index as $W_i(\mathbf{k}^*)$. This approach can provide acceptable results in cases where the system is not very heterogeneous or where permeability is of high correlation length in the plane normal to the well trajectory in the near-well region.

With more highly heterogeneous permeability fields, the simple $W_i(\mathbf{k}^*)$ treatment described above can lead to considerable error. In such cases, it is necessary to compute upscaled well indices and, for additional accuracy, near-well transmissibilities between the well block and adjacent blocks. The first such near-well upscaling procedure was presented by Ding [24]. Subsequent approaches were presented in [30, 62, 66]. We now describe the basic ideas behind these near-well upscaling techniques.

We define a local problem with $r = 1$ (where r again designates the number of bordering rings of coarse block regions) with the well block in the center, as shown in Fig. 5. Rather than impose boundary conditions that lead to an approximately linear flow, we solve the dimensionless fine scale pressure equation with a well source term q^w in the central block:

$$\nabla \cdot (\mathbf{k} \cdot \nabla p) = q^w. \tag{36}$$

In the discretized form of this equation, q_i^w is represented using Eq. (33). We specify a wellbore pressure of $p_i^w = 1$ and a pressure on the outer boundary of $p = 0$. The solution of Eq. (36) can then be computed to determine pressure and velocity in all of the fine grid blocks in the extended local problem.

Following this fine grid solution, we estimate the coarse grid well index, designated W_i^*, and coarse scale well block transmissibilities (i.e., transmissibilities linking the well block to adjacent blocks), designated T_w^*, as follows. We first compute the volume averaged pressure $\langle p \rangle_i$ in the well block and each of its four neighbors via application of Eq. (30). The flow rates through each of the four interfaces linking the well block to adjacent blocks (designated q_1 - q_4) are computed using Eq. (31). We can then calculate the coarse scale parameters W_i^* and T_w^* via:

$$W_i^* = \frac{q^w}{\langle p \rangle_i - p_i^w}, \tag{37}$$

and

$$(T_w^*)_{i+1/2} = \frac{q_1}{\langle p \rangle_i - \langle p \rangle_{i+1}}, \tag{38}$$

where $q^w = q_1 + q_2 + q_3 + q_4$. In two dimensions, four T_w^* are computed - one corresponding to each connection between the well block and neighboring blocks (in three dimensions there are six T_w^*).

The use of these parameters in many cases provides significantly improved coarse scale representations of well performance. In some cases, it has proved useful [62] to introduce coarse scale iteration to force the fluxes computed from the local coarse scale problem to agree with the integrated fine scale fluxes q_1 - q_4. This is accomplished by iterating on the coarse scale parameters W_i^* and T_w^* until an objective function based on the mismatch in flux between the fine and coarse problems is minimized. This minimization was achieved in [62]using a Gauss-Newton procedure.

5   Global and quasi global upscaling procedures

The methods described in §4 – local and extended local procedures – all require the specification of (assumed) boundary conditions on the local problem. In global upscaling methods, by contrast, the intent is to solve a global flow problem and to use this solution to extract coarse scale quantities.

5.1   Global upscaling techniques

Some examples of global upscaling methods are those presented by White and Horne [92], Pickup *et al.* [71], Nielsen and Tveito [67], Holden and Nielsen [47] and Aarnes [1]. Most of these methods apply transmissibility upscaling for the calculation of coarse grid quantities. From the fine grid solution, transmissibilities are computed by averaging over coarse block regions and then applying Eq. (32). This gives a first estimate for all of the T^*. In highly heterogeneous models, a significant fraction of these transmissibilities may be negative. Iteration is therefore performed until all of the transmissibilities are positive and a sufficient level of agreement between the fine and coarse solutions is achieved [47]. Various quantities (pressure, velocity, flux) can be considered during these iterations and different approaches focus on different variables.

Global upscaling methods can provide very accurate results for a particular set of wells and boundary conditions. In many cases the model developed in this way can be used for other (sufficiently similar) flow scenarios. However, it is also possible that the model may lack robustness with respect to other boundary conditions or well arrangements (see, e.g., Holden *et al.* [48] and Chen and Durlofsky [15] for some results addressing this issue).

A technique that shares some similarities with global upscaling methods is multigrid upscaling [65]. In multigrid upscaling, coarse scale parameters are determined at a specified level from the multigrid solution algorithm. It will be of interest to compare multigrid and global upscaling techniques in detail to obtain a better understanding of the commonalities and differences between the two approaches.

5.2   Local-global (quasi global) upscaling

Quasi global upscaling methods attempt to estimate the effects of the global flow without actually solving a global fine scale problem. Here we will briefly outline the quasi global procedures developed by Chen *et al.* [16], Chen and Durlofsky [15] and Wen *et al.* [86], referred to as local-global approaches. The idea of these methods is to use global coarse scale simulations to estimate the boundary conditions to use in the extended local calculation of T^* (we will describe the method within the context of T^* upscaling, though it is also applicable for $\mathbf{k}^*$ upscaling). The procedure is iterated until the upscaled quantity is consistent with the global flow (i.e., self-consistency is enforced).

Two variants of the general local-global approach have been developed. In the coupled local-global approach of Chen *et al.* [16], generic global boundary conditions are employed (i.e., pressure boundary conditions are applied to drive flow across the entire domain). In [15] and [86], by contrast, an "adaptive local-global" procedure, in which flow is driven by specific global boundary conditions and/or wells, is applied. With this approach, the upscaled model is adapted to a particular global flow. Near-well upscaling, as described in §4.6, is automatically incorporated into the calculations. The adaptive local-global upscaling method includes a thresholding procedure which assures that local calculations are only performed for a portion of coarse blocks during the iterations. This leads to computational efficiency and eliminates (or significantly reduces) the appearance of anomalous (e.g., negative or extremely large) T^* values.

The coupled local-global and adaptive local-global techniques share many similarities, though the adaptive procedure, because it provides upscaled quantities tuned for a particular well configuration, is the more accurate. The adaptive procedure does, however, require that a portion of the upscaled quantities be recomputed if well locations change. Our description here is for the adaptive local-global technique, though the basic procedure is similar for the coupled approach. The technique is illustrated schematically in Fig. 6. The first step is the local or extended local calculation of T^* using any of the boundary conditions discussed above (e.g., pressure - no flow or periodic). This provides the initial estimate of the upscaled quantities. Using the coarse scale model generated in this way, a global simulation is then performed to provide the global coarse scale pressure field (designated via the $\times$'s in Fig. 6a). This pressure field is then used to set boundary conditions for the extended
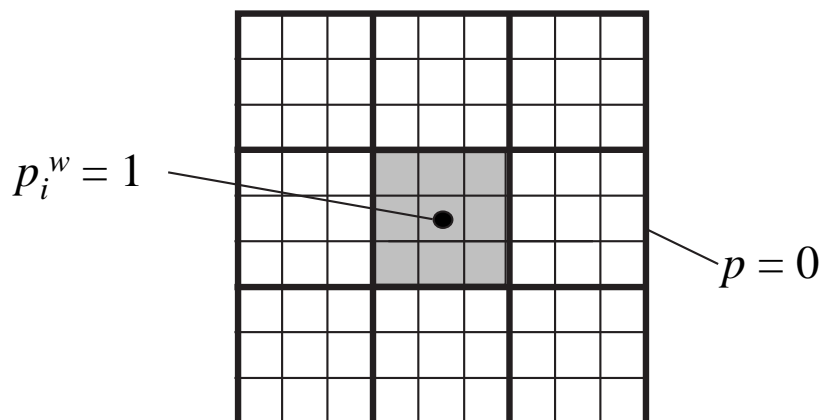
Figure 5: Schematic for near-well upscaling showing fine (finer lines) and coarse (heavier lines) grids in the near-well region ($r = 1$).
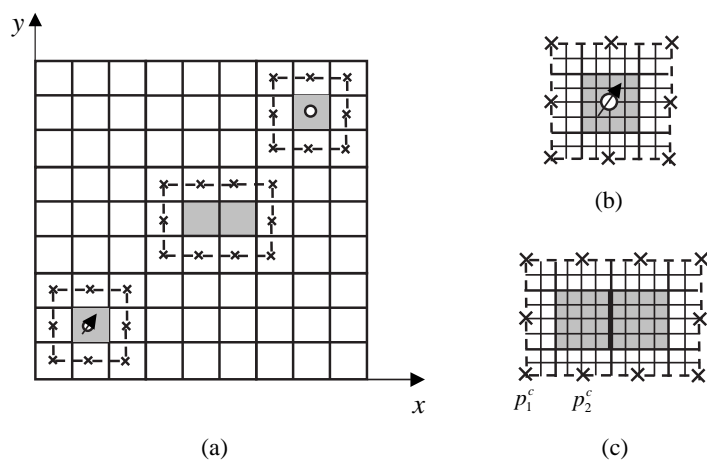

Figure 6: Schematic of adaptive local-global upscaling showing (a) coarse scale global domain with global flow driven by wells, (b) fine scale local near-well region, and (c) fine scale local region away from wells. The ×'s represent coarse pressures (from [15]).

local problems for the calculation of T^* (and W^* for well blocks). These extended local calculations are illustrated in Figs. 6b and c. Iteration proceeds in this way until the upscaled quantities no longer change with iteration, at which point the global flow field and T^* are consistent.

In order to actually solve the extended local problems at each iteration, the coarse global pressure field must be interpolated to provide local boundary conditions on the fine grid. This is accomplished via a simple linear interpolation. As with any extended local, quasi global or global approach, this procedure can on occasion provide negative T^*. In order to minimize (or eliminate) the appearance of such anomalous T^*, a thresholding procedure is applied during the iterations. Specifically, T^* is recomputed only for interfaces subject to coarse scale flow rates that exceed $\epsilon q_c^{\max}$, where $q_c^{\max}$ is the global maximum flow rate for similarly oriented interfaces and ϵ is an algorithmic parameter.

The three-dimensional implementation of adaptive local-global upscaling described in [86] employs reduced border regions, which leads to substantial gains in computational efficiency. Specifically, in [86] it is shown that the use of purely local upscaling for the initial T^* estimate, in conjunction with the use of border regions comprised of two rings of fine cells during the iterations, provides results in close agreement with those from the "full" adaptive local-global procedure (the full procedure includes border regions comprised of all of the fine cells contained within a ring of coarse cells around the target cell or interface). Three-dimensional results using the reduced border region implementation will be presented below.

6   Flow-based gridding techniques

Until this point we have considered the calculation of the upscaled parameters $\mathbf{k}^*$, T^* and W^*. The accuracy of the upscaled model can often be improved considerably through the use of specialized gridding techniques. In particular, the use of flow-based gridding in conjunction with accurate upscaling procedures represents a powerful approach for the generation of coarse scale models that retain the geological realism of the fine grid description. The basic goal of these methodologies is the introduction of higher levels of grid refinement in high flow regions of the model and coarser descriptions in lower flow regions. This allows the coarsened model to capture many important effects of the fine scale permeability field without retaining a uniformly fine grid. Grid generation techniques can also be use to capture geological features (such as faults) or to better resolve well trajectories.

Flow-based gridding procedures have been developed by a variety of investigators, both within Cartesian and curvilinear grid frameworks. Durlofsky *et al.* [28, 29] presented a nonuniform coarsening technique that selectively removes fine scale grid lines in a manner that retains important high flow regions. This approach, applied

in both two and three dimensions, is appropriate within the context of Cartesian or stratigraphic grids. However, it is limited because the coarse grid is constrained to be aligned with (i.e., overlay) the fine grid. More general flow-based gridding procedures are not constrained in this way because they allow the coarse grid to be non-aligned with respect to the underlying fine (geocellular) grid.

Within the context of reservoir simulation, a number of procedures for flow-based grid generation have been presented. Verma and Aziz [85], Edwards *et al.* [34], Portella and Hewett [73], Castellini *et al.* [13, 12], Wen *et al.* [87] and He [44] presented techniques based on the use of streamlines computed from a single-phase flow solution of the fine scale problem. An alternate gridding procedure, based on the grouping of cells of similar permeability, was suggested by Garcia *et al.* [38]. These researchers introduced the concept of an "elastic grid," in which the grid is adjusted to minimize the variance of permeability within coarse grid cells. Other investigations along these lines include the work of Ebrahimi and Sahimi [31] and earlier papers discussed by Farmer [37]. In related work by Tran [84] and Wen and Gómez-Hernández [91], the general approach of Garcia *et al.* [38] was combined with flow information to generate flow-based grids.

Many of the previous techniques for flow-based grid generation were limited to two-dimensional systems. Of the work cited here, only Castellini *et al.* [13, 12] and He [44] developed procedures for curvilinear grid generation in three-dimensional systems.

The generation of flow-based grids has also been addressed within the context of groundwater hydrology. In this setting, flow-based grids may be applied either for the solution of the contaminant transport equation or for the efficient solution of the pressure equation. Relevant papers along these lines include Cirpka *et al.* [19] and Cao and Kitanidis [11]. Cirpka *et al.* applied flow-based grids for the solution of the contaminant transport equation, while Cao and Kitanidis developed an unstructured flow-based gridding procedure for the solution of the pressure equation. Their procedure entails the use of an a posteriori error estimate to guide grid refinement. Within an unstructured grid context, there have been a number of other flow-based grid generation procedures. These include the PEBI windowing techniques of Mlacnik *et al.* [64, 63] as well as the triangle-based procedure developed by Edwards [33]. Flow-based gridding for fully unstructured models in three dimensions was considered by Prevost *et al.* [74, 76].

Grid generation is a very broad area, with applications in many areas of scientific and engineering computing. Extensive discussions of the general area can be found in the books by Thompson *et al.* [83] and Knupp and Steinberg [58]. Elliptic and optimization-based grid generation techniques, such as those described by Knupp and coworkers [56, 57], can make use of flow information and have the potential to provide coarse grids with a relatively high degree of control on internal grid geometry. In recent work, He [44] explored the application of these more general procedures

to reservoir simulation problems. This work is discussed below in §6.2.

6.1 Streamline-based gridding procedures

Methods based directly on the use of streamline information may provide grids with an extremely high concentration of grid lines in high flow regions, particularly in highly heterogeneous systems. Here we describe flow-based grid generation techniques that use streamline information, though a grid-smoothing step is introduced to provide more control over the local grid density, which acts to improve grid quality. This capability introduces a higher degree of flexibility into the overall grid generation procedure.

The description here follows the presentation in Wen *et al.* [87]. The first step in the flow-based grid generation procedure is the solution of the single-phase incompressible pressure equation over the fine grid region. The pressure equation, repeated here,

$$\nabla \cdot (\mathbf{k} \cdot \nabla p) = 0 \, , \tag{39}$$

can be solved over either the entire geocellular model or over only some portion of it. In the latter case, the global problem must first be decomposed into a number of sub-domains or modules. Although the fine grid permeability field can be described on any type of grid, it is commonly defined on a Cartesian or stratigraphic grid. The fine grid permeability may be isotropic, a diagonal tensor or a full tensor quantity. The coarse grid models will here be characterized by irregular quadrilateral (in two dimensions) or hexahedral (in three dimensions) cells and full tensor permeabilities in the general case.

Although the generation of a flow-based grid requires the solution of a fine scale problem, this calculation often represents a fairly small computational cost relative to the solution of the two-phase (or multiphase) system on either the fine or coarse scale. This is because Eq. (39) is only solved once, while the two-phase flow problem requires the solution of the pressure equation at every time step. If the fine scale solution of Eq. (39) over the entire flow domain is prohibitive, then the grid generation can be accomplished in a modular fashion. Following the generation of the grid in each module, the modules can be recombined into either a single globally structured grid or a multiblock (or modular) grid (see Jenny *et al.* [51] for examples of grids of this type). Here we describe the basic grid generation procedure for a single domain.

The basic idea of the grid generation procedure is to use streamlines to define the high flow paths and to introduce refinement in these areas. Although the grid is determined using flow-based information from a single fine grid solution, it is usually appropriate for use in a variety of related flow problems. We describe the grid generation procedure with reference to a two-dimensional flow domain in an

$x - y$ coordinate system. The flow-based grid is formed by first solving Eq. (39) subject to $p = 1$ on the left face ($x = 0$), $p = 0$ on the right face ($x = L_x$) and no flow on the $y = 0$ and $y = L_y$ boundaries, where L_x and L_y denote the system lengths in the x and y directions. Following this solution, streamlines can be generated through either a particle tracking technique (Thiele *et al.* [82]) or through the contouring of the streamfunction Ψ. The particle tracking technique is more general, in that it can be applied in two and three dimensions, while the streamfunction technique is only appropriate in two dimensions. However, when the flow is driven by boundary conditions (rather than by wells), as is the case here, the two-dimensional streamfunction can be easily computed from the velocity field in a post-processing step using:

$$\Delta \Psi = \int_l \mathbf{u} \cdot \mathbf{n} \, dl \, , \tag{40}$$

where $\Delta \Psi$ is the increment in streamfunction between two cell corners and l is the cell edge connecting the two nodes. Because the quantity $\mathbf{u} \cdot \mathbf{n}$ is known accurately (and conservatively) along cell edges from the flux-continuous finite volume solution, this is a viable approach for determining streamfunction. Streamlines are then generated as lines of constant Ψ. Some number of streamlines is then selected to provide one set of coordinate lines.

The other coordinate lines can be obtained from isopotentials (contours of constant pressure) or from streamlines generated from a complementary flow problem (e.g., flow from $y = 0$ to $y = L_y$ with no flow on $x = 0$ and $x = L_x$). Another approach is to divide each of the streamline coordinate lines into a specified number of segments of equal arc length and to simply connect these segments.

Grids generated directly from streamlines introduce high levels of resolution in regions of high flow. This approach can result in grids with highly distorted cells and an overly high concentration of grid lines in high flow regions (and very few grid lines in lower flow regions). This can present difficulties if the grid is applied to problems that differ from that used to define the streamlines. For example, if the grid is to be used to study the effects of well placement, then the grid must be applicable for a variety of different flow problems. To provide grids with more uniformity, it is useful to apply some amount of grid smoothing.

The basic idea of grid smoothing is to control the level of grid line concentration throughout the domain. The procedure described here is relatively simple, though more complex variants can be readily defined. Following the solution of Eq. (39) on the fine scale in an $x - y$ coordinate system and the determination of the initial coordinate lines, the x and y locations of all of the grid line intersections can be determined. These intersections, designated $x_{i,j}$ and $y_{i,j}$, provide the locations of the corner points of each coarse cell.

The grid smoothing now entails some number of Laplacian-type iterations of the

form:

$$x_{i,j}^{k+1} = (1 - \omega)x_{i,j}^k + \frac{1}{4}\omega(x_{i-1,j}^k + x_{i+1,j}^k + x_{i,j-1}^k + x_{i,j+1}^k)\,, \qquad \text{(41a)}$$

$$y_{i,j}^{k+1} = (1 - \omega)y_{i,j}^k + \frac{1}{4}\omega(y_{i-1,j}^k + y_{i+1,j}^k + y_{i,j-1}^k + y_{i,j+1}^k)\,, \qquad \text{(41b)}$$

where $(x_{i,j}^k, y_{i,j}^k)$ with $k = 1$ designates the initial grid, $(x_{i,j}^{k+1}, y_{i,j}^{k+1})$ designates subsequent (smoothed) grids and ω is a relaxation parameter $(0 < \omega \le 1)$. For clarity, we here use two subscripts for the grid block index. In the two dimensional examples below, we used anywhere from 2-5 iterations of Eqs. (41) with $\omega = 0.6$.

We now present an example illustrating the smoothing procedure. The permeability field for a channel system is depicted in Fig. 7 (this permeability field is from [61]). The initial coordinate lines, generated as described above, are shown in Fig. 8. The grid is clearly highly concentrated in some regions and very coarse in other regions. A more uniform grid, generated using two smoothing iterations, is displayed in Fig. 9.
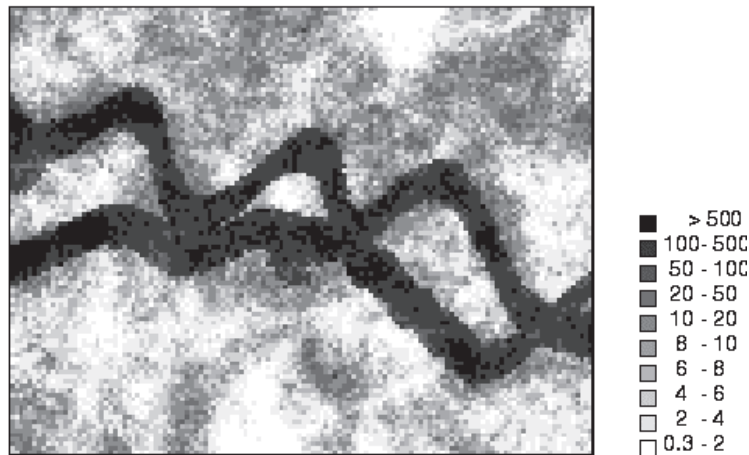
Figure 7: Permeability field for fluvial reservoir.

This grid is better suited for flow calculations. The final step in the grid generation procedure is to upscale the geocellular permeabilities to the cells of the flow-based grid. This can be accomplished using the procedure described in §4.5.

Flow-based grids in three dimensions can be constructed using a similar approach to that described above. A streamline-based coordinate system is again established as the initial grid, though the procedure is more involved in three dimensions. Smoothing is again applied to improve grid quality if necessary. Two related but distinct techniques for three-dimensional streamline-based grid generation are presented by Castellini *et al.* [13, 12] and He [44].
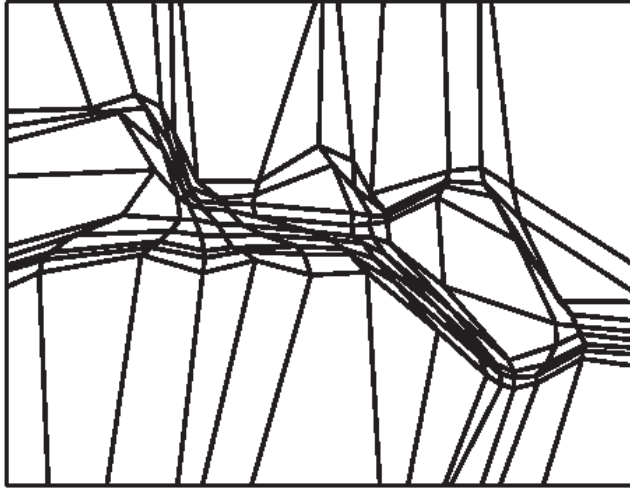
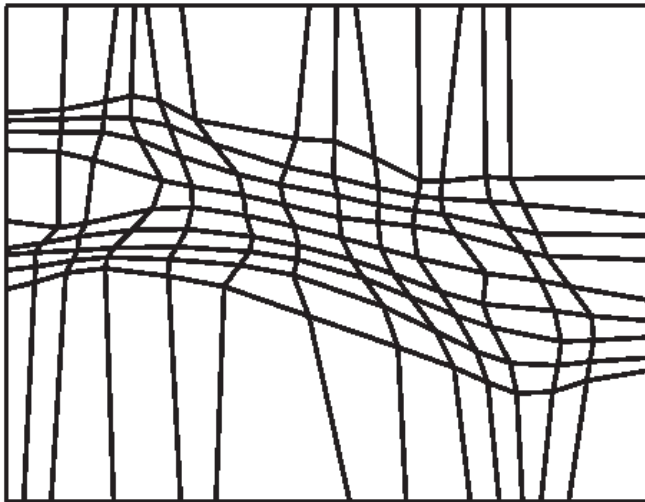Figure 8: Initial flow-based grid for permeability field of Fig. 7 (from [87]).

Figure 9: Final flow-based grid after smoothing (from [87]).

6.2 Elliptic grid generation techniques

Elliptic grid generation techniques entail the solution of nonlinear elliptic equations for the determination of the mapping from logical space to physical space. In this context, logical space can be thought of as a unit cube (in three dimensions), while physical space refers to the actual simulation model. The description here closely follows that of He [44].

The grid generation process provides the transformation

$$\mathbf{x}(\boldsymbol{\xi}) : \boldsymbol{\xi}^n \rightarrow \mathbf{x}^n, \tag{42}$$

where n is the dimensionality, $\mathbf{x}$ represents the coordinates in physical space and $\boldsymbol{\xi}$ represents the coordinates in logical space. Elliptic grid generation methods solve elliptic equations with $\mathbf{x}$ as the dependent variables and $\boldsymbol{\xi}$ as the independent variables to obtain this transformation numerically. Boundary points are usually specified, meaning that Dirichlet boundary conditions are prescribed for the elliptic solutions.

The mapping in Eq. (42) can be quantified in terms of the Jacobian matrix of the transformation $\mathcal{J}$. In the simple case of planar grids in two dimensions, the Jacobian matrix is defined as:

$$\mathcal{J} = \left[\begin{array}{cc} \mathcal{J}_{11} & \mathcal{J}_{12} \\ \mathcal{J}_{21} & \mathcal{J}_{22} \end{array} \right] = \left[\begin{array}{cc} x_\xi & x_\eta \\ y_\xi & y_\eta \end{array} \right], \tag{43}$$

where $x_\xi = \partial x / \partial \xi$, etc. The determinant of $\mathcal{J}$ is referred to as the Jacobian J of the mapping ($J = det\mathcal{J} = x_\xi y_\eta - x_\eta y_\xi$). The Jacobian matrix in general varies with location over the domain. In order to obtain one-to-one mappings, $J \neq 0$ is required. In discrete form, J is proportional to the area of a cell. This mapping can also be expressed through the so-called metric tensor $\mathcal{G}$, which is directly related to the Jacobian matrix via $\mathcal{G} = \mathcal{J}^T \mathcal{J}$. The determinant of $\mathcal{G}$ is referred to as the metric g, with $g = J^2 = (x_\xi y_\eta - x_\eta y_\xi)^2$ or $J = \sqrt{g}$.

The grid generation techniques applied here are based on the concept of "reference Jacobian matrices" or simply "reference Jacobians," designated $\mathcal{J}_{ref}$. The idea here is that we have a set of $\mathcal{J}_{ref}$ (as a function of position) that we want the grid to honor. These reference Jacobians might derive from flow information in some portions of the domain (e.g., they can be determined from a streamline-based grid generated as described previously) or they might be prescribed in such a way as to resolve key geometric features (such as a well or fault). We can then construct a grid that fits these Jacobian matrices in a "least-square" sense. Because the mapping involves a least-square fit, some inconsistencies in the $\mathcal{J}_{ref}$ are permitted.

Starting from the variational principle, an elliptic grid generation procedure based on reference Jacobians is derived by Knupp [56]. The equations to be solved

in two dimensions are

$$g_{22}\mathbf{x}_{\xi\xi} - 2g_{12}\mathbf{x}_{\xi\eta} + g_{11}\mathbf{x}_{\eta\eta} = -\sqrt{g}\mathcal{J}\mathbf{R}, \tag{44}$$

where g_{11}, g_{12} and g_{22} are the components of $\mathcal{G}$ and

$$\mathbf{R} = \left[\begin{array}{c} (\mathcal{S}_{11})_{\xi}y_{\eta} - (\mathcal{S}_{12})_{\xi}x_{\eta} - (\mathcal{S}_{11})_{\eta}y_{\xi} + (\mathcal{S}_{12})_{\eta}x_{\xi} \\ (\mathcal{S}_{21})_{\xi}y_{\eta} - (\mathcal{S}_{22})_{\xi}x_{\eta} - (\mathcal{S}_{21})_{\eta}y_{\xi} + (\mathcal{S}_{22})_{\eta}x_{\xi} \end{array} \right] \tag{45}$$

with $\mathcal{S} = \mathcal{J}_{ref}^{-1}$. For further details on the method (in two and three dimensions) and the numerical implementation, see [44].

We can use the elliptic grid generation method to combine different kinds of information. As an example, we combine flow and geological information, as shown in Fig. 10. The plot in the upper left shows a grid generated by a streamline-based method while that in the lower left shows a fault resolved using the Jacobian-based method. Starting from the upper left grid (which is used to define $\mathcal{J}_{ref}$ over most of the domain), and modifying the $\mathcal{J}_{ref}$ in the region near the feature (as in the lower left plot in Fig. 10), we solve Eq. (44) to obtain a grid that combines the two types of information, as shown in the grid on the right in Fig. 10. We can also apply this procedure to generate grids that combine information from multiple flow scenarios in order to form grids that are less dependent on one particular flow.

6.3 Assessing the quality of the upscaled model

In this section we will assume that the upscaled model is defined by the flow-based grid and the cell $\mathbf{k}^*$ or T^*, computed using the methods described earlier. The upscaled model is intended to capture, to the extent possible, the effects of key geological and geometric features. Because the fine scale multiphase flow model may be overly time consuming to actually simulate even once, it is often difficult to assess the quality of the coarse scale description. We now briefly discuss some strategies for assessing the accuracy of the coarse model and describe an approach for model iteration. In assessing the upscaled model, the idea is to simulate a problem that is representative of the fine scale problem without simulating the actual fine scale model. One means of accomplishing this is to simulate unit mobility ratio displacements, as described in [29].

In a unit mobility ratio displacement, the displacing phase has properties identical to those of the displaced phase. This model is much faster to run than an actual two or three-phase flow problem because the pressure and velocity fields do not change during the course of the simulation. Thus, the pressure equation need be solved only once on the fine scale. The unit mobility ratio case can be recovered from the two-phase equations by setting the oil viscosity equal to the water viscosity and the relative permeabilities equal to the phase saturation; i.e., $k_{rw} = S$, $k_{ro} = 1 - S$,

Streamline-Based Method
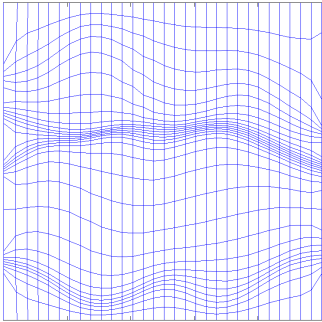
Jacobian-Based Method
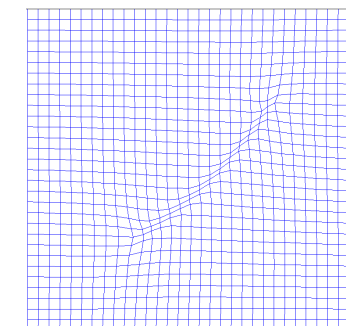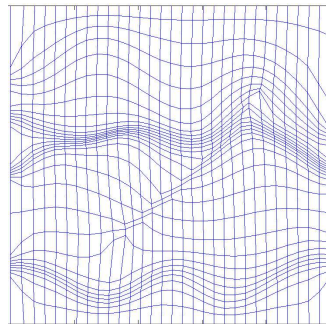
Jacobian-Based Method

Figure 10: Combining flow information and feature resolution using a Jacobian-based grid generation method (from [44]).

where S is water saturation. In this case, the dimensionless pressure equation is identical to Eq. (39). The equation describing the movement of the individual phase fronts within the reservoir, the saturation equation, is then given by:

$$\frac{\partial S}{\partial t} + \nabla \cdot (\mathbf{u}S) = 0 \, , \tag{46}$$

where ϕ is assumed to be constant. Because the velocity field does not vary in time, this equation can be solved very efficiently and accurately by integrating along streamlines (e.g., Prevost *et al.* [75]). The Darcy velocity must first be computed by applying Darcy's law to the pressure field ($\mathbf{u} = -\mathbf{k} \cdot \nabla p$).

The solutions of Eqs. (39) and (46) can be used as "diagnostics" to assess the accuracy of the upscaled model. Although these equations differ from the actual flow equations, they do capture many important aspects of two-phase (or multiphase) flow problems. Specifically, the effects of heterogeneity are often similar in the unit mobility and two-phase flow problems.

Various quantities can be compared between the fine and coarse scale solutions of Eqs. (39) and (46). The two that are perhaps the most representative of the general level of accuracy of the upscaled model are the global (overall) flow rate and the fractional flow of displaced fluid (e.g., oil cut) at the outlet (or production well) as a function of pore volume injected. The global flow rate through the model can be quantified in terms of the global equivalent permeability, K_g. For global flow in the x direction, driven by pressure boundary conditions at $x = 0$ and $x = L_x$, this quantity is given by:

$$K_{g,x} = \frac{Q_x L_x}{L_y L_z \Delta p} \, , \tag{47}$$

where Δp is the difference in pressure between $x = 0$ and $x = L_x$ and Q_x is the total flow rate through the system in the x direction. For global flow in the y or z directions, similar expressions can be obtained. The grid structure can be iterated until the agreement in these two (or similar) quantities is acceptable. A number of different coarse grid structures can be compared to the fine grid solution relatively efficiently since the fine grid solution of Eq. (39) need only be computed once.

The overall gridding, upscaling and diagnostic procedure described above is illustrated schematically in Fig. 11 for a two-dimensional system. The first step here is the solution of a single-phase fine grid flow problem. This solution is used both as the reference solution (against which coarse scale simulation results will be compared) and in the grid generation procedure. Next, a grid is formed and $\mathbf{k}^*$ or T^* is computed for the coarse scale cells (using any of the methods discussed above). Following this, a global coarse scale flow problem is solved and the result compared to the fine scale reference solution. Iteration on the grid structure can be used to improve the agreement with the fine scale solution.

34

Fine grid model (**k**, ϕ)

1. Perform fine grid single phase flow calculation (streamlines)

2. Form coarse grid structure

3. Compute coarse grid properties ($\mathbf{k}^*$, ϕ^*)

4. Compare fine (—) and coarse (- - -) grid flow results
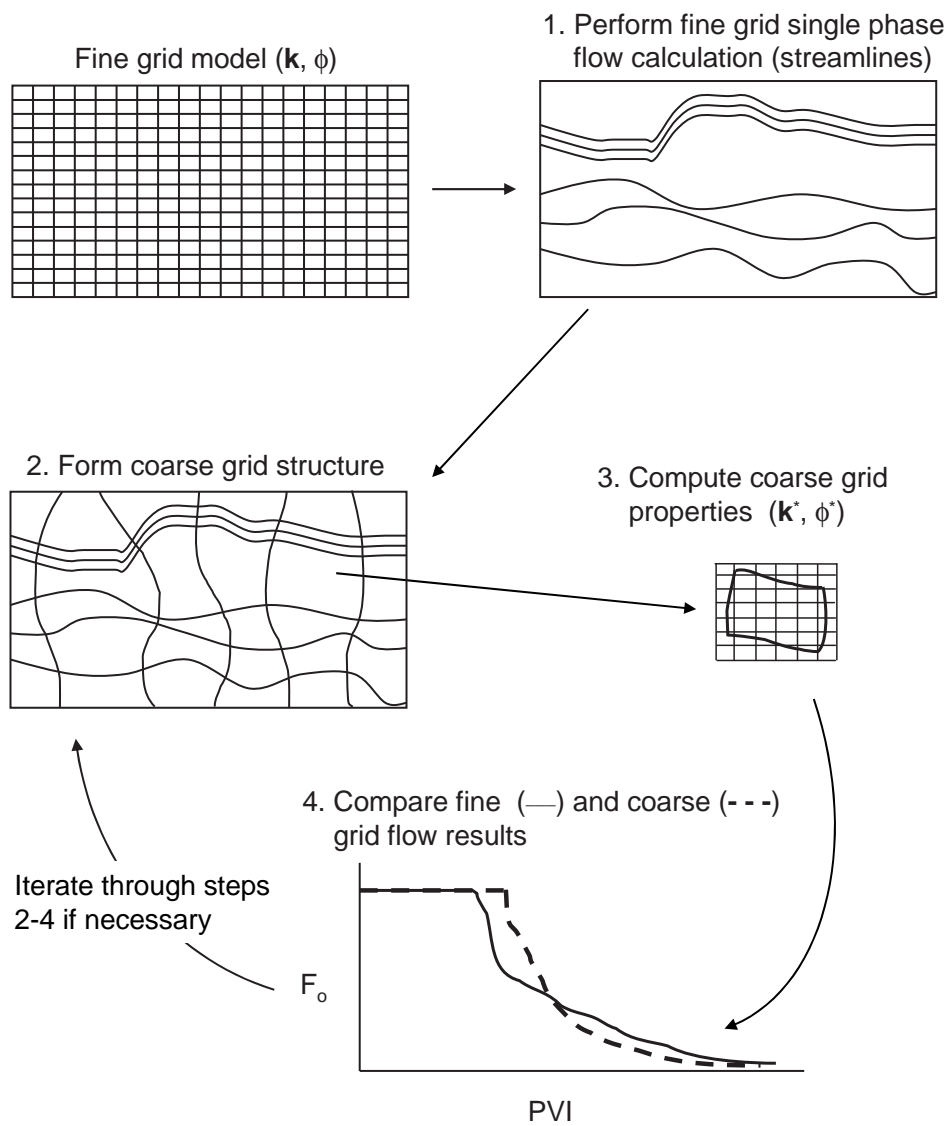
Iterate through steps 2-4 if necessary

F_o

PVI

Figure 11: Schematic illustrating iterative grid generation procedure and use of flow diagnostics.

These diagnostics are computationally inexpensive within the context of flow-based gridding procedures since fine scale flows are already computed in the grid generation step. The ability to perform an efficient and accurate assessment of the coarse scale model represents a significant advantage for flow-based gridding techniques over other grid generation procedures that are not based on fine scale flow solutions. As a final check on the accuracy of the coarse model, it is useful to perform a multiphase flow simulation of a portion of the fine scale model and compare this solution to that for the corresponding region of the coarse scale model. This provides an assessment of the accuracy of the coarse scale model in terms of multiphase flow effects.

7   Numerical upscaling results

We now present upscaling results for a number of systems. In several of these examples we use the North Sea channelized system presented in Christie and Blunt [17]. In other cases we use geostatistical models generated using GSLIB algorithms (Deutsch and Journel [22]). Most of the results discussed in this section were presented previously in recent papers and theses (e.g., [62, 87, 88, 44, 86]). The results presented here are not intended to be exhaustive but rather illustrative of the performance of the various techniques for different geological models. Some of these results are presented in terms of total flow rate through the system for a prescribed pressure difference (i.e., Q or $K_{g,x}$, as defined in Eq. (47)).

7.1   Local and extended local upscaling for highly heterogeneous systems

In the case of two-point geostatistical models (e.g., spherical variogram models), when the permeability correlation directions are oriented with the simulation grid, purely local upscaling techniques have been shown to perform well in terms of maintaining the total flow through the model. For example, for two-dimensional systems of this type, if we upscale by about a factor of 5 in each coordinate direction (giving a coarse grid with a factor of 25 fewer grid blocks than the fine grid), $K_{g,x}$ computed from the coarse model will typically show errors of less than 10% relative to the reference fine scale calculation (see results in [29, 89, 45]). In these cases, the use of extended local procedures (i.e., border regions, as described in §4.4) does not appear to lead to significantly improved coarse scale results [89]. For models of this type, improved transport results (e.g., oil cut), relative to those obtained using uniformly coarsened grids, can be achieved using flow-based nonuniform grid coarsening within a Cartesian grid framework [29, 28]. The observations that border regions do not offer much improvement but that Cartesian-based nonuniform coarsening procedures

do provide enhanced accuracy for transport are both related to the fact that the correlation structure of the permeability field is aligned with the simulation grid.
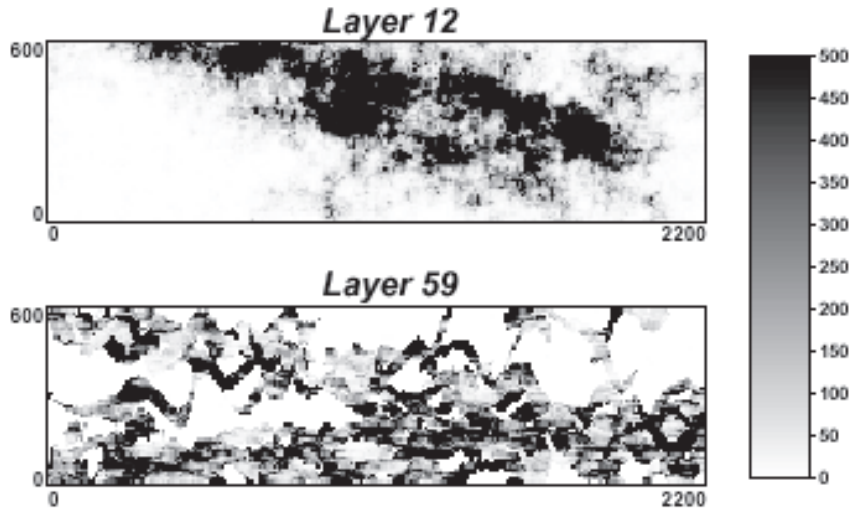

Figure 12: Continuous and channelized layers from North Sea reservoir (model from [17]).

Border regions often do provide enhanced accuracy when the correlation structure of the permeability field is not aligned with the grid or when the permeability field is characterized by multipoint geostatistics. We illustrate the potential improvement in coarse model accuracy offered through the use of border regions with results from [88]. These calculations use the model of [17]. This model is of dimensions $60 \times 220 \times 85$. The upper 35 layers display a somewhat continuous permeability field, while the lower 50 layers are highly channelized (representative layers are shown in Fig. 12). We illustrate the impact of border regions by considering each layer to be a two-dimensional system, of dimensions 220×60, which is upscaled to 22×20 (note that the x and y directions are now switched relative to that specified in [17] such that the longer dimension is here the x direction). Results are presented as scatter plots, with $K_{g,x}$ for each coarsened layer plotted against $K_{g,x}$ for the same layer simulated using the fine scale permeability field. A perfect upscaling would give all of the points on the 45° line.

In the first set of results, the models are upscaled using a purely local procedure ($r = 0$) and periodic boundary conditions. Very similar results were obtained using pressure - no flow boundary conditions, so the effect of the boundary conditions in this case is small [88]. From Fig. 13, we see that the coarse scale results for the layers with the continuous permeability fields, indicated by open circles on the figure, are
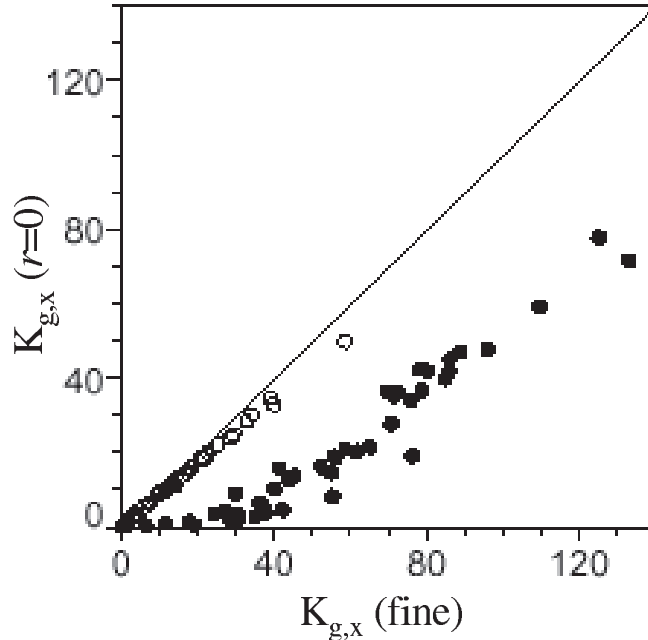
Figure 13: Cross plot of $K_{g,x}$ from coarse model ($r = 0$) against $K_{g,x}$ from fine model. Open circles correspond to continuous layers, solid circles to channelized layers (from [88]).

in close agreement with the fine scale results. Errors for the lower layers, designated by solid circles, are by contrast quite substantial. For all of the data in Fig. 13, the average relative error is 46%.

Fig. 14 displays results using the extended local upscaling ($r = 1$) using periodic boundary conditions (though again very similar results were obtained using pressure - no flow boundary conditions). We see considerable improvement in the coarse scale results for the channelized layers. The average relative error for all of the data is reduced to 27% in this case. This error is still significant, though it does represent a clear improvement over that of Fig. 13.

Part of the error in the coarse scale results in Figs. 13 and 14 is due to numerical discretization effects rather than upscaling effects. We can gauge the relative magnitudes of these two effects by refining the grid (back to 220×60) in the upscaled models while retaining the 22×20 coarse scale permeability field (i.e., we project the coarse scale permeability field onto the fine grid). Results for 220×60 models of this type with the coarse permeability field generated using $r = 1$ are shown in Fig. 15. The error here is reduced considerably relative to that in Fig. 14 (average relative error is here 16%). This illustrates that a significant portion of what is considered
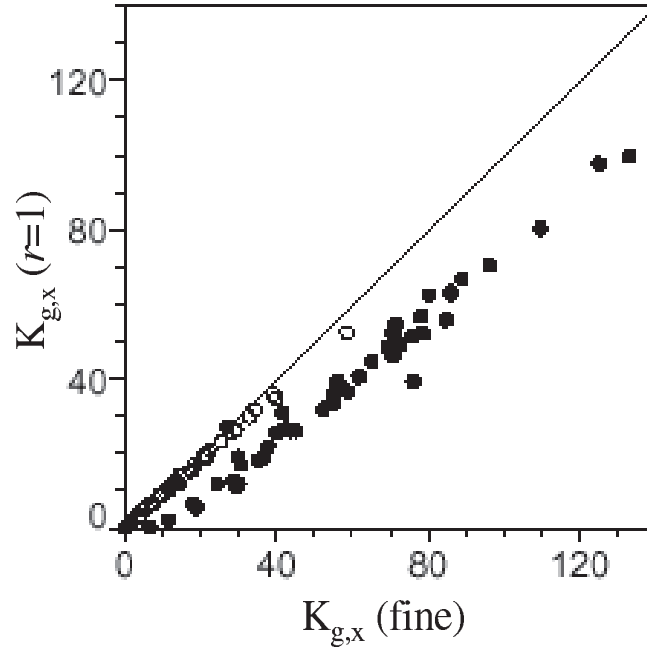
Figure 14: Cross plot of $K_{g,x}$ from coarse model ($r = 1$) against $K_{g,x}$ from fine model (from [88]).

to be "upscaling error" may really be due to numerical discretization effects rather than to inaccuracy introduced in the calculation of $\mathbf{k}^*$.

We note finally that transmissibility upscaling (using an extended local procedure) was found to provide better overall accuracy than permeability upscaling for the difficult channelized cases in [17]. This may be because transmissibility upscaling avoids the additional approximations introduced in computing transmissibilities from $\mathbf{k}^*$ via Eq. (13). The local-global procedure illustrated below applies transmissibility upscaling for this reason.

7.2 Near-well upscaling

We illustrate the potential impact of near-well heterogeneity, and the importance of capturing these effects in coarse scale models, through an example from [62]. This example involves a horizontal well in a complex three dimensional sand-shale reservoir containing an oil zone, an aquifer and a gas cap. This case was considered previously by Aziz *et al.* [5] who used this system to illustrate the effects of fine scale heterogeneity on horizontal well performance.
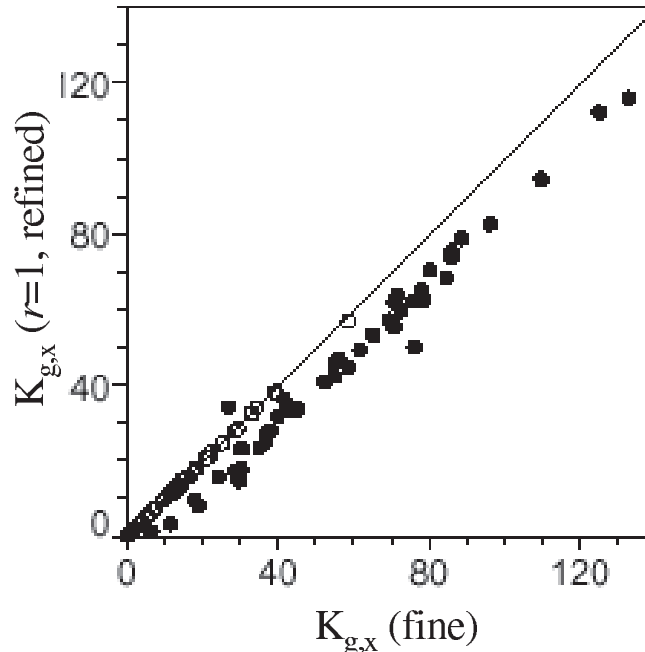
Figure 15: Cross plot of $K_{g,x}$ computed on 220×60 grid using $\mathbf{k}^*$ from coarse model ($r = 1$) against $K_{g,x}$ from fine model (from [88]).

The fine scale reservoir model contains $100 \times 50 \times 32$ cells and is described in [5]. The coarse model, of dimensions $25 \times 25 \times 12$, was generated through a uniform coarsening of the fine scale model using a local upscaling method, with an additional layer retained in both the aquifer and gas cap. The single horizontal producer was specified to produce at a target rate of 5000 bbl/day, with a minimum bottom hole pressure constraint of 1500 psi.

Results for oil rate for the fine model, the coarse model using a well index computed directly from the upscaled permeability (i.e., $W_i(\mathbf{k}^*)$ using the terminology of §4.6) and the coarse model with near-well upscaling (W_i^* and T_w^*) are shown in Fig. 16. The coarse results without the near-well treatment are clearly in considerable error relative to the reference fine scale results. This is mainly due to the fact that the coarse model in this case continues to produce at the target rate for a period of time that is 10 times too long. The coarse model with the near-well upscaling, by contrast, provides a much more accurate pressure response and, as a result, switches to bottom hole pressure control at about the correct time. This behavior is evident from the pressure profiles shown in Fig. 17. The upscaled model with the near-well treatment also provides accurate results for water cut. Results for GOR, though much more accurate than coarse scale results without near-well
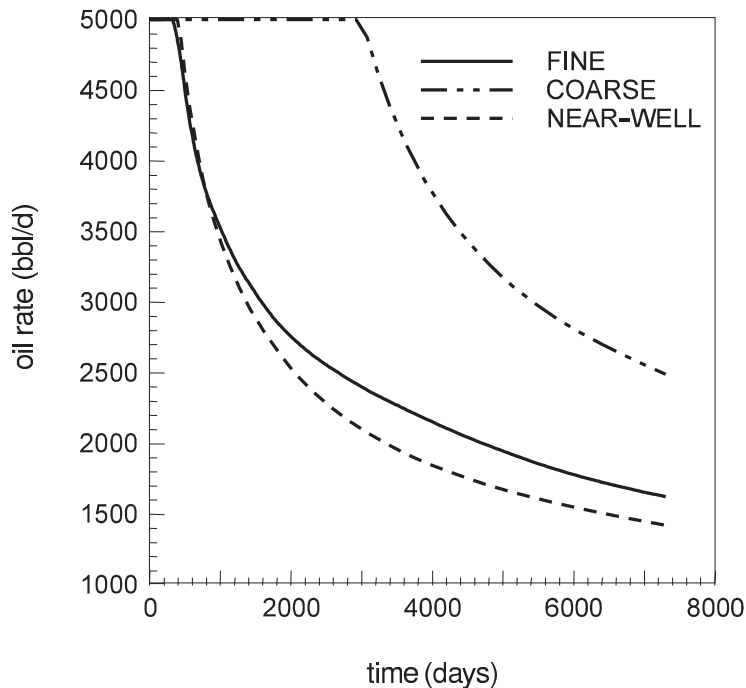
Figure 16: Oil production rate (three-phase flow) for sand - shale system (from [62]).

upscaling, are not as accurate. Results for both water cut and GOR are presented in [62].

7.3   Adaptive local-global upscaling

We next illustrate the improvement in results that can be attained using the adaptive local-global upscaling procedure described in §5.2. Extensive numerical results are presented in [16, 15, 86, 14]; the results shown here represent a small sample. We consider channelized systems from the model in [17], as discussed above. The examples presented here are from Wen *et al.* [86].

The first example involves a two-dimensional system. The permeability field, shown in Fig. 18a, is layer 73 (of dimensions 220×60) from [17]. Pressure boundary conditions are imposed at the lower left and upper right of the model, over regions indicated by the heavy lines in Fig. 18a. The total flow rate Q through the fine scale model is 11.02 (in dimensionless terms). The fine scale model is upscaled uniformly to 22×6. Shown in Figs. 18b - 18d are comparisons between fine scale and coarse scale results for pressure. The fine scale results, shown in Fig. 18b, are first averaged onto the coarse grid and then contoured.
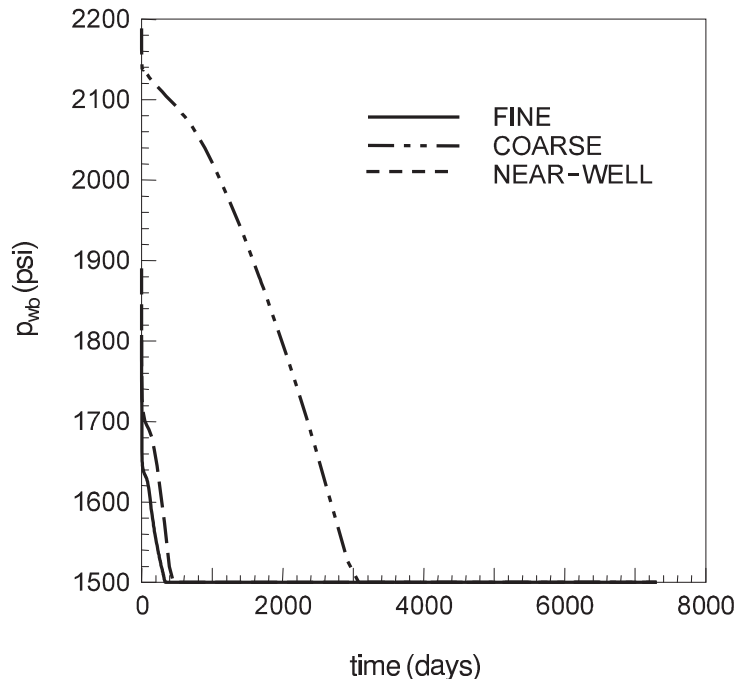
Figure 17: Wellbore pressure for sand - shale system (from [62]).

The pressure field determined from a coarse scale model generated using extended local T^* upscaling (with constant pressure - no flow local boundary conditions) is shown in Fig. 18c. Because local upscaling is unable to capture the effects of large scale permeability connectivity for this system, the upscaled result shows considerable error relative to the fine scale solution. The total flow rate computed from this model is 4.60, an error of 58%. Results using adaptive local-global upscaling (with two iterations) are shown in Fig. 18d. These results are very close to the averaged fine scale results and clearly represent a significant improvement over extended local T^* upscaling. In terms of total flow rate, the model generated using adaptive local-global upscaling gives $Q = 10.77$, which is within 2.3% of the fine scale solution.

We next consider a three-dimensional system and illustrate the performance of "reduced" adaptive local-global upscaling (in which no border regions are used in the initial T^* calculation and border regions containing two rings of *fine* cells are used during the iterations). This system contains the 50 channelized layers from the model considered above (from [17]) and is of dimension $60 \times 220 \times 50$ (in this example, the x and y directions are now as specified in [17]). The coarsened model is $12 \times 44 \times 10$ (upscaling ratio of 125).

Using the well arrangement specified in [17], errors in well flow rates using all of

42

(a) Channelized permeability field (layer 73)

(b) Contours of averaged fine scale pressure

(c) Contours of coarse pressure from
extended local T^*

(d) Contours of coarse pressure from
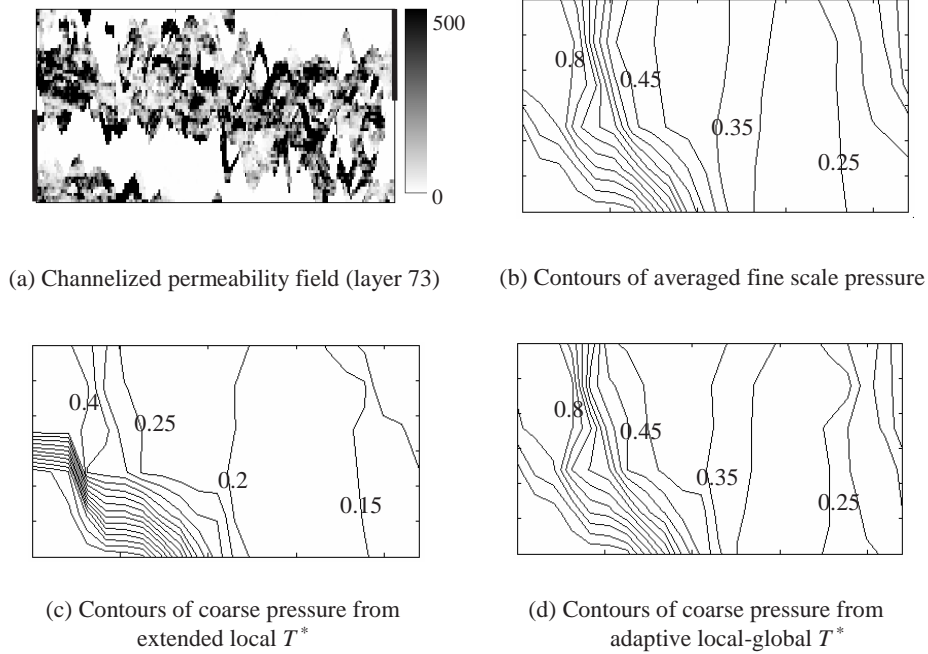adaptive local-global T^*

Figure 18: Permeability field (from [17]) and pressure profiles for fine and coarsened models (from [86]).

the upscaling techniques were relatively small. We therefore employ a different well arrangement than was specified in the original problem. Specifically, an injection well I is located at (5, 216), production well P1 is located at (55, 6) and production well P2 is located at (5, 46). The permeability field and well locations are shown in Fig. 19.

Results for well flow rates computed using models upscaled with different procedures are shown in Table 1. Flow rates are normalized with respect to the injection rate in the fine model. For this case, errors using both extended local $\mathbf{k}^*$ upscaling ($r = 1$, no near-well upscaling) and extended local T^* upscaling ($r = 1$, with near-well upscaling) are large. Specifically, errors in injection rate are 46% and 24% respectively and errors in P2 are 79% and 47%. The use of full adaptive local-global (ALG) upscaling (with $r = 1$) decreases the errors substantially - error in injection rate is now 4.2% and the error in P2 is 5.8%. The use of the reduced adaptive local-global procedure provides a similarly high degree of accuracy. Using ALG (reduced), the maximum flow rate error is actually decreased relative to the full adaptive local-global procedure, presumably due to the effects of random errors (maximum error is now 1.8%). The accuracy of these results and those in the two-dimensional example
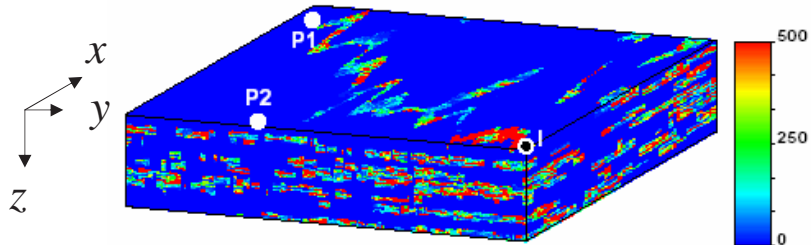
Figure 19: Permeability field and well locations for channelized system (model adapted from [17]).

(Fig. 18) demonstrate that high degrees of accuracy can be obtained even though a two-point flux approximation is used in local-global upscaling. This highlights the fact that, although technically a multipoint flux approximation is required (due to full-tensor effects), the more efficient two-point approximation suffices in many cases.

The last column in Table 1 displays timings for the various upscaling procedures. These timings are normalized with respect to the timing for the full adaptive local-global upscaling procedure. It is apparent from the table that ALG (reduced) requires less computation than any of the other methods (all of which incorporate all of the fine cells corresponding to a ring of coarse cells around the target region) and is of comparable accuracy to ALG (full). This suggests that the reduced adaptive local-global upscaling procedure may represent an accurate and efficient technique for practical reservoir simulation problems.

Table 1: Flow results for permeability field and well configuration of Fig. 19.

Model	I	P1	P2	CPU
Fine	1	0.395	0.605	–
$\mathbf{k}^*$ only	0.543	0.413	0.130	0.64
T^* + nwsu	0.759	0.438	0.321	0.65
ALG (full)	1.042	0.402	0.640	1
ALG (reduced)	0.990	0.396	0.594	0.24

7.4   Flow-based gridding and upscaling

We illustrate flow-based gridding and upscaling with an example from Wen *et al.* [87]. This case involves a permeability field with oriented layers, generated using

Gaussian sequential simulation [22]. The permeability field is of dimensions 100×100 and displays layering (and principal axes of permeability) oriented at an angle θ of 30° relative to the x axis. The correlation length along the direction of the layering is $0.8L$ while the correlation length normal to the layering is $0.04L$, where $L = L_x = L_y$ is the length of a side of the (square) domain. Permeability is log-normally distributed, with the variance of $\log k$ equal to 4. In each fine scale block we set $k_2 = 0.1k_1$, where k_1 is the principal value of permeability in the direction along the layering and k_2 is the principal value of permeability in the direction across the layering. The permeability in the $x - y$ coordinate system is therefore a full tensor quantity, which can be determined from k_1 and k_2 in each block and θ via:

$$\mathbf{k}(x,y) = \left[\begin{array}{cc} k_1 \cos^2 \theta + k_2 \sin^2 \theta & (k_1 - k_2) \sin \theta \cos \theta \\ (k_1 - k_2) \sin \theta \cos \theta & k_1 \sin^2 \theta + k_2 \cos^2 \theta \end{array} \right], \qquad (48)$$

where $\theta = 30°$. The permeability field is shown in Fig. 20 ($\log(k_1)$ is the scalar quantity actually displayed in the figure). The flow-based grid for this case is of dimensions 20×20. This grid, shown in Fig. 21, was generated using the technique described in §6.1. Upscaled permeabilities were computed using the finite volume method described in §4.5.
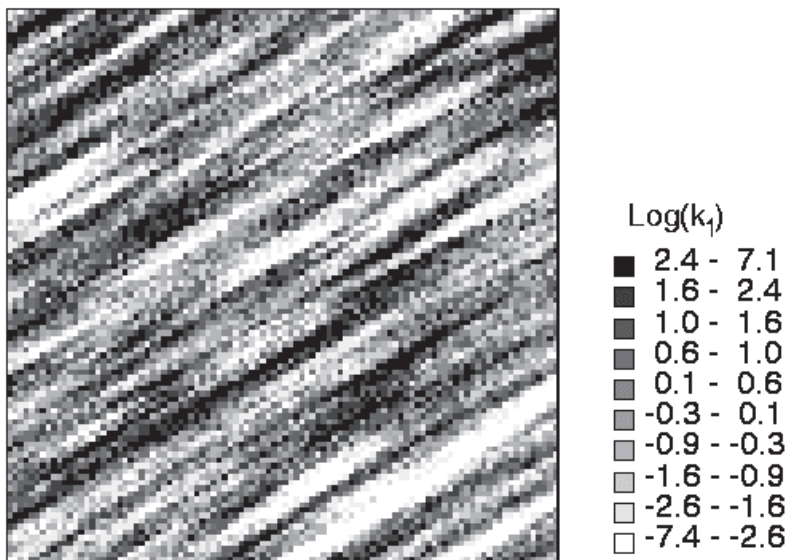

Figure 20: Permeability field with layering oriented at 30° (from [87]).

The simulation in this case involves two-phase flow. Relative permeabilities to water and oil are specified as $k_{rw} = S^2$ and $k_{ro} = (1 - S)^2$ and the viscosity ratio (μ_o/μ_w) is 10. The total mobility therefore varies in time, which means that the pressure equation (10) and the saturation equation (9) must be solved at each time
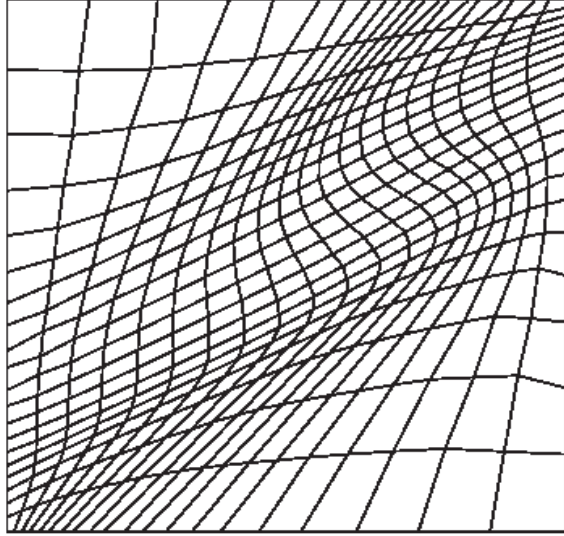
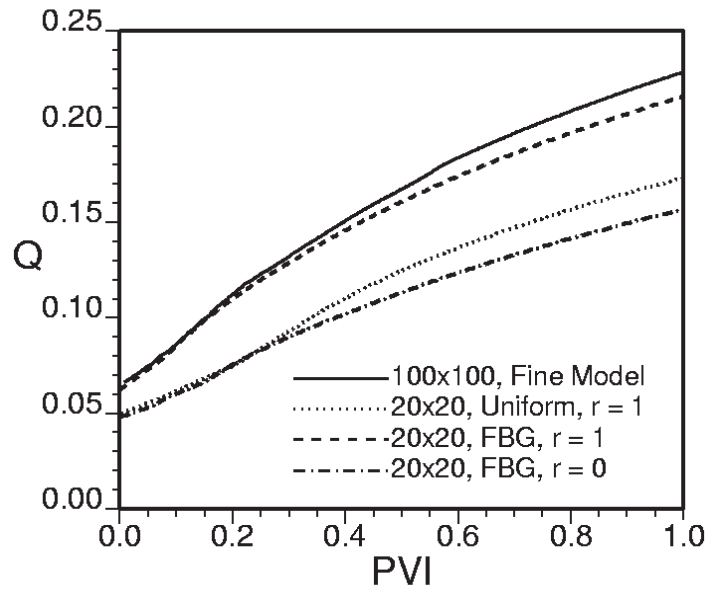Figure 21: Flow-based grid after smoothing for permeability field of Fig. 20 (from [87]).

Figure 22: Total flow rate for two-phase flow in the x direction in oriented system (from [87]).
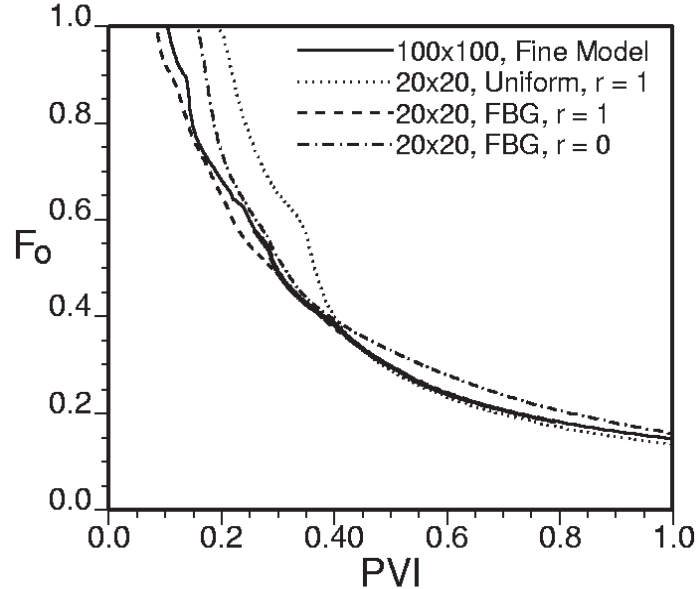
Figure 23: Oil cut for two-phase flow in the x direction in oriented system (from [87]).

step (an IMPES procedure is applied). Flow in this case is in the x direction and is driven by boundary conditions of the same form as those used to generate the initial streamlines. We fix $S = 1$ at the inlet edge of the model for these simulations.

Results for total flow rate (Q) as a function of time (PVI) are shown in Fig. 22. Four curves are shown in the figure. These correspond to the 100×100 fine grid solution (solid curve), the 20×20 uniform coarse grid solution generated using $r = 1$ (dotted curve), the flow-based grid solution with $\mathbf{k}^*$ computed with $r = 0$ (dot-dash curve), and the flow-based grid solution with $\mathbf{k}^*$ computed with $r = 1$ (dashed curve). The flow-based grid results, with $\mathbf{k}^*$ computed using $r = 1$, are in close agreement with the fine grid results (at initial time, the error is about 5%). This is in contrast to the uniform grid results with $r = 1$ and to the flow-based grid results with $\mathbf{k}^*$ computed using $r = 0$ (initial time errors for both of these results are more than 20%).

Results for oil cut (F_o) versus PVI are shown in Fig. 23. Again we see the best accuracy using the flow-based grid with $\mathbf{k}^*$ computed using $r = 1$, though breakthrough does occur slightly earlier than in the fine scale solution. This may be due to numerical dispersion effects. The uniform grid predicts late breakthrough, as does the flow-based grid with $\mathbf{k}^*$ computed using $r = 0$ (though error is less in this case). The results of Figs. 22 and 23 demonstrate that a grid formed by solving a single-phase flow problem can still be used within the context of a two-phase flow
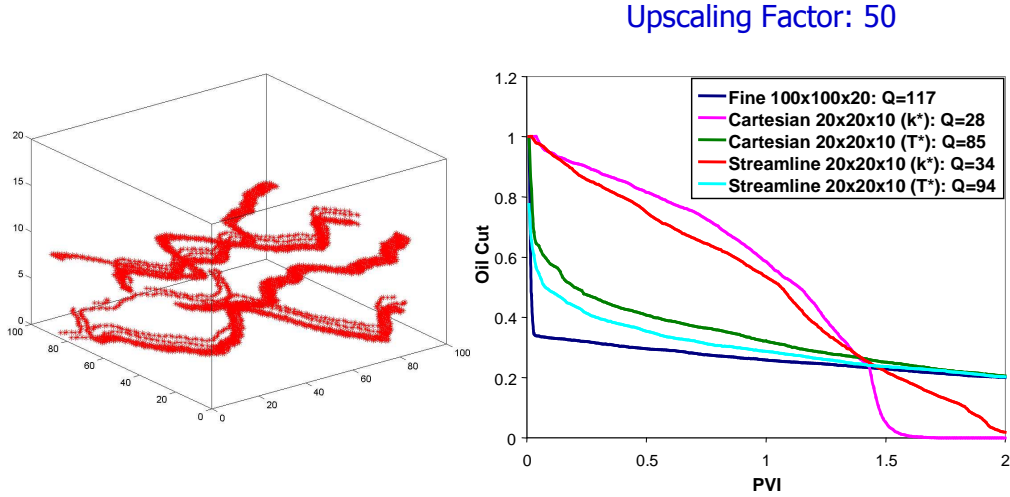
47

Figure 24: Multiple-channel system in three-dimensions: left - permeability field; right - flow results (from [44]).

simulation. It is important to note that the coarse scale flow-based grid model required a factor of 60 times less computation time than the fine model. These savings will be realized each time the coarse model is run. The grid generation and permeability upscaling calculations required only about 0.4% of the fine grid simulation time, so the overhead cost is quite small for this problem.

Our final example (from He [44]) involves the use of a streamline-based grid for a channelized system in three-dimensions. The channelized system, shown in Fig. 24, is generated using FLUVISM, an object-based geostatistical tool [23]. This tool allows the user to specify the maximum number of channels, channel width, thickness and sinuosity ranges, orientations, etc. Indicator-type data are generated and permeabilities are assigned accordingly (here we assign 1000 md for the sand and 1 md for the background regions). This type of permeability field is highly discontinuous and the flow is for the most part in the channels.

The fine model is of dimensions $100 \times 100 \times 20$ and the coarse models are $20 \times 20 \times 10$ (upscaling factor of 50). Results are shown for both Cartesian and streamline-based grids and for both $\mathbf{k}^*$ and T^* upscaling (a global method based on a two-point flux approximation is used in this case for T^* upscaling; see [44] for details). The cyan curve in Fig. 24 (flow-based grid plus transmissibility upscaling) gives the closest result compared to the fine results. Here the upscaling method plays the more significant role in the accuracy of the results in terms of both oil cut and total flow rate Q. Specifically, it is the use of the more accurate T^* upscaling technique that most impacts coarse grid accuracy in this case. This is because the streamline grid is limited in terms of its ability to resolve the multiple (and sinuous) high-flow

channels. The use of the streamline grid does, however, provide improvement for both oil cut and total flow rate.

8 Concluding remarks and future directions

In this paper, techniques for upscaling detailed geocellular models were described and applied. The methods discussed include local, extended local, global and quasi global procedures for computing upscaled permeability or transmissibility, techniques for upscaling to irregular quadrilateral cells, upscaling in the vicinity of wells, and the use of flow-based gridding procedures for capturing the effects of connected permeability in coarse models.

The various upscaling methods were shown to provide coarse scale results of varying levels of accuracy. For example, for the North Sea permeability field considered in [17], it was shown that purely local permeability upscaling provided accurate coarse scale results for the upper, more continuous layers. The coarse models generated in this way were not nearly as accurate, however, for the lower channelized layers. For these layers, the use of border regions in the upscaling improved the coarse scale results considerably. The adaptive local-global procedure was shown to further enhance the results for highly heterogeneous reservoirs. Near-well upscaling, which can be applied as an extended local technique or within the context of adaptive local-global upscaling, was shown to provide improvement in modeling wells. The benefits of smoothed flow-based grids were illustrated using a permeability field that was oriented relative to the underlying coordinate system. In this case it was demonstrated that the combined use of the flow-based grid and border region upscaling provided the most accurate overall results. Flow-based gridding combined with transmissibility upscaling was also shown to be very effective for the coarse modeling of a channelized system in three dimensions.

The upscaling of two-phase flow functions (e.g., calculation of pseudo relative permeabilities) was not discussed in this review. As indicated in the Introduction, such upscaling will be required when high degrees of coarsening are applied. In addition, this type of upscaling may also be necessary when additional two-phase flow effects (such as effective coarse scale capillary pressure functions) are required.

A number of techniques were described and illustrated individually in this paper. It will be of interest to investigate hybrid procedures that combine one or more of the methods described here to give a more powerful overall upscaling methodology. Potentially useful combinations include the use of local-global upscaling in conjunction with flow-based gridding as well as the coupling of many of the techniques described here with approaches for two-phase upscaling. Extension of many of the techniques presented here to unstructured models is also of great interest. In addition, if many geological models are to be considered, it is important that the

gridding and upscaling techniques be further (or completely) automated.

Finally, it is very important that we achieve a better understanding of the error introduced by the various upscaling procedures. By quantifying this error through the development of error models, we will be able to determine the appropriate upscaling method and level of coarsening to use for a particular problem. Error models can also be used to correct predictions made using coarse models. Progress in the general area of error modeling has been reported by [41, 60, 68] among others, though the techniques have thus far been applied only for idealized problems. The development of practical methods to assess and model upscaling error will allow for the use of coarse scale simulations with the appropriate level of model complexity.

Acknowledgments

Nomenclature

A	area
f	fractional flow function
F_o	oil cut
$\mathbf{G}$	arbitrary pressure gradient
$\mathcal{G}$	metric tensor
$\mathcal{J}$	Jacobian matrix of grid transformation
$\mathbf{k}$	permeability tensor
$\mathbf{k}^*$	effective or equivalent permeability tensor
k_{rj}	relative permeability for phase j
K_g	global equivalent permeability
l	dimensionless correlation length
L	system length
m	mass flow rate
$\mathbf{n}$	normal vector
p	pressure
q	volumetric flow rate
Q	global flow rate

r	size of border region or radius
S	saturation
t	time
T	transmissibility
$\mathbf{u}$	Darcy velocity
V	volume
W_i	well index for block i
$\mathbf{x}$	slow (coarse) scale or physical space coordinates
$\mathbf{y}$	fast (fine) scale
ϕ	porosity
λ	mobility
μ	viscosity
θ	layer orientation
ρ	density
σ	standard deviation
ω	power averaging exponent, relaxation parameter
$\boldsymbol{\xi}$	logical space coordinates
Ψ	streamfunction

Subscripts

b	bulk
i	block index
j	phase or block index
l	fine block index
o	oil
ref	reference
t	total
w	water or well
x, y, z	coordinate direction

Superscripts

$\tilde{}$	per unit volume
$*$	upscaled, effective or equivalent
c	coarse scale
j	flow solution (1 or 2)
k	iteration number
w	well

References

[1] J. E. Aarnes. *On Numerical Methods for Multifield Problems and Fast Reservoir Performance Prediction.* Ph.D. thesis, University of Bergen, Norway, 2002.

[2] I. Aavatsmark, T. Barkve, O. Boe, and T. Mannseth. Discretization on non-orthogonal, quadrilateral grids for inhomogeneous, anisotropic media. *Journal of Computational Physics*, 127:2–14, 1996.

[3] M. Abbaszadeh and N. Koide. Evaluation of permeability upscaling techniques and a new algorithm for interblock transmissibilities. SPE paper 36179, presented at the 7th Abu Dhabi International Petroleum Exhibition & Conference, Abu Dhabi, UAE, Oct. 13-16, 1996.

[4] T. Arbogast and S. L. Bryant. A two-scale numerical subgrid technique for waterflood simulations. *SPE Journal*, 7:446–457, 2002.

[5] K. Aziz, S. Arbabi, and C.V. Deutsch. Why is it so difficult to predict the performance of horizontal wells? *Journal of Canadian Petroleum Technology*, 38:37–45, 1999.

[6] K. Aziz and A. Settari. *Petroleum Reservoir Simulation.* Applied Science Publishers, 1979.

[7] J. W. Barker and P. Dupouy. An analysis of dynamic pseudo-relative permeability methods for oil-water flows. *Petroleum Geoscience*, 5:385–394, 1999.

[8] J. W. Barker and S. Thibeau. A critical review of the use of pseudo-relative permeabilities for upscaling. *SPE Reservoir Engineering*, 12:138–143, 1997.

[9] O. Boe. Analysis of an upscaling method based on conservation of dissipation. *Transport in Porous Media*, 17:77–86, 1994.

[10] A. Bourgeat. Homogenized behavior of two-phase flows in naturally fractured reservoirs with uniform fractures distribution. *Computer Methods in Applied Mechanics and Engineering*, 47:205–216, 1984.

[11] J. Cao and P. K. Kitanidis. Adaptive-grid simulation of groundwater flow in heterogeneous aquifers. *Advances in Water Resources*, 22:681–696, 1999.

[12] A. Castellini. *Flow Based Grids for Reservoir Simulation.* M.S. report, Stanford University, Stanford, CA, 2001.

[13] A. Castellini, M. G. Edwards, and L. J. Durlofsky. Flow based modules for grid generation in two and three dimensions. 7th European Conference on the Mathematics of Oil Recovery, Baveno, Italy, Sept. 5-8, 2000.

[14] Y. Chen. *Upscaling and Subgrid Modeling of Flow and Transport in Heterogeneous Reservoirs.* Ph.D. thesis, Stanford University, Stanford, CA, 2005.

[15] Y. Chen and L. J. Durlofsky. Adaptive local-global upscaling for general flow scenarios in heterogeneous formations. *To appear in Transport in Porous Media*, 2005.

[16] Y. Chen, L. J. Durlofsky, M. Gerritsen, and X. H. Wen. A coupled local-global upscaling approach for simulating flow in highly heterogeneous formations. *Advances in Water Resources*, 26:1041–1060, 2003.

[17] M. A. Christie and M. J. Blunt. Tenth SPE comparative solution project: a comparison of upscaling techniques. *SPE Reservoir Evaluation & Engineering*, 4:308–317, 2001.

[18] M.A. Christie. Upscaling for reservoir simulation. *Journal of Petroleum Technology*, 48:1004–1010, 1996.

[19] O. A. Cirpka, E. O. Frind, and R. Helming. Streamline-oriented grid generation for transport modelling in two-dimensional domains including wells. *Advances in Water Resources*, 22:697–710, 1999.

[20] N. H. Darman, G. E. Pickup, and K. S. Sorbie. A comparison of two-phase dynamic upscaling methods based on fluid potentials. *Computational Geosciences*, 6:5–27, 2002.

[21] C. V. Deutsch. Calculating effective absolute permeability in sandstone/shale sequences. *SPE Formation Evaluation*, 4:343–348, 1989.

[22] C. V. Deutsch and A. G. Journel. *GSLIB: Geostatistical Software Library and User's Guide.* 2nd edition, Oxford University Press, New York, 1998.

[23] C. V. Deutsch and T. T. Tran. FLUVSIM: a program for object-based stochastic modeling of fluvial depositional systems. *Computers & Geosciences*, 28:525–535, 2002.

[24] Y. Ding. Scaling up in the vicinity of wells in heterogeneous field. SPE paper 29137, presented at the SPE Reservoir Simulation Symposium, San Antonio, TX, Feb. 12-15, 1995.

[25] L. J. Durlofsky. Upscaling of geocellular models for reservoir flow simulation: a review of recent progress. 7th International Forum on Reservoir Simulation, Bühl/Baden-Baden, Germany, June 23-27, 2003.

[26] L. J. Durlofsky. Numerical calculation of equivalent grid block permeability tensors for heterogeneous porous media. *Water Resources Research*, 27:699–708, 1991.

[27] L. J. Durlofsky. Coarse scale models of two phase flow in heterogeneous reservoirs: volume averaged equations and their relationship to existing upscaling techniques. *Computational Geosciences*, 2:73–92, 1998.

[28] L. J. Durlofsky, R. A. Behrens, R. C. Jones, and A. Bernath. Scale up of heterogeneous three dimensional reservoir descriptions. *SPE Journal*, 1:313–326, 1996.

[29] L. J. Durlofsky, R. C. Jones, and W. J. Milliken. A nonuniform coarsening approach for the scale up of displacement processes in heterogeneous media. *Advances in Water Resources*, 20:335–347, 1997.

[30] L. J. Durlofsky, W.J. Milliken, and A. Bernath. Scale up in the near-well region. *SPE Journal*, 5:110–117, 2000.

[31] F. Ebrahimi and M. Sahimi. Multiresolution wavelet scale up of unstable miscible displacements in flow through heterogeneous porous media. *Transport in Porous Media*, 57:75–102, 2004.

[32] M. G. Edwards. Superconvergent renormalization and tensor approximation. 5th European Conference on the Mathematics of Oil Recovery, Z. E. Heinmann, ed., Leoben, Austria, Sept. 3-6, 1996.

[33] M. G. Edwards. Unstructured, control-volume distributed, full-tensor finite-volume schemes with flow based grids. *Computational Geosciences*, 6:433–452, 2002.

[34] M. G. Edwards, R. Agut, and K. Aziz. Quasi K-orthogonal streamline grids: gridding and discretization. SPE paper 49072, presented at the SPE Annual Technical Conference and Exhibition, New Orleans, LA, Sept. 27-30, 1998.

[35] M. G. Edwards and C. F. Rogers. Finite volume discretization with imposed flux continuity for the general tensor pressure equation. *Computational Geosciences*, 2:259–290, 1998.

[36] C. F. Eek-Jensen, I. Aavatsmark, and O. Boe. Upscaling on general quadrilateral grids in 3D with application to field cases. Proceedings of the EAGE - 10th European Symposium on Improved Oil Recovery, Brighton, UK, Aug. 18-20, 1999.

[37] C. L. Farmer. Upscaling: a review. *International Journal for Numerical Methods in Fluids*, 40:63–78, 2002.

[38] M. H. Garcia, A. G. Journel, and K. Aziz. Automatic grid generation for modeling reservoir heterogeneities. *SPE Reservoir Engineering*, 7:278–284, 1992.

[39] Y. Gautier, M. J. Blunt, and M. A. Christie. Nested gridding and streamline-based simulation for fast reservoir performance prediction. *Computational Geosciences*, 3:295–320, 1999.

[40] M. G. Gerritsen and L. J. Durlofsky. Modeling fluid flow in oil reservoirs. *Annual Review of Fluid Mechanics*, 37:211–238, 2005.

[41] J. Glimm, S. L. Hou, H. J. Kim, Y. Lee, D. H. Sharp, K. Ye, and Q. S. Zou. Risk management for petroleum reservoir production: a simulation-based study of prediction. *Computational Geosciences*, 5:173–197, 2001.

[42] J. J. Gómez-Hernández and A. G. Journel. Stochastic characterization of grid block permeability. *SPE Formation Evaluation*, 9:93–99, 1994.

[43] D. R. Guérillot and S. Verdière. Different pressure grids for reservoir simulation in heterogeneous reservoirs. SPE paper 29148, presented at the SPE Reservoir Simulation Symposium, San Antonio, TX, Feb. 12-15, 1995.

[44] C. He. *Structured Flow-based Gridding and Upscaling for Reservoir Simulation*. Ph.D. thesis, Stanford University, Stanford, CA, 2004.

[45] C. He, M. G. Edwards, and L. J. Durlofsky. Numerical calculation of equivalent cell permeability tensors for general quadrilateral control volumes. *Computational Geosciences*, 6:29–47, 2002.

[46] L. Holden and O. Lia. A tensor estimator for the homogenization of absolute permeability. *Transport in Porous Media*, 8:37–46, 1992.

[47] L. Holden and B. F. Nielsen. Global upscaling of permeability in heterogeneous reservoirs: the Output Least Squares (OLS) method. *Transport in Porous Media*, 40:115–143, 2000.

[48] L. Holden, B. F. Nielsen, and S. Sannan. Upscaling of permeability using global norms. 7th European Conference on the Mathematics of Oil Recovery, Baveno, Italy, Sept. 5-8, 2000.

[49] T. Y. Hou and X. H. Wu. A multiscale finite element method for elliptic problems in composite materials and porous media. *Journal of Computational Physics*, 134:169–189, 1997.

[50] P. Jenny, S. H. Lee, and H. A. Tchelepi. Multi-scale finite-volume method for elliptic problems in subsurface flow simulation. *Journal of Computational Physics*, 187:47–67, 2003.

[51] P. Jenny, C. Wolfsteiner, S. H. Lee, and L. J. Durlofsky. Modeling flow in geometrically complex reservoirs using hexahedral multiblock grids. *SPE Journal*, 7:149–157, 2002.

[52] E. Kasap and L. W. Lake. Calculating the effective permeability tensor of a gridblock. *SPE Formation Evaluation*, 5:192–200, 1990.

[53] M. J. King, D. G. MacDonald, S. P. Todd, and H. Leung. Application of novel upscaling approaches to the Magnus and Andrew reservoirs. SPE paper 50643, presented at the SPE European Petroleum Conference, The Hague, The Netherlands, Oct. 20-22, 1998.

[54] M. J. King and M. Mansfield. Flow simulation of geologic models. *SPE Reservoir Evaluation & Engineering*, 2:351–367, 1999.

[55] P. R. King. The use of renormalization for calculating effective permeability. *Transport in Porous Media*, 4:37–58, 1989.

[56] P. Knupp. Jacobian-weighted elliptic grid generation. *SIAM Journal of Scientific Computing*, 17:1475–1490, 1996.

[57] P. Knupp, L.G. Margolin, and M. Shashkov. Reference Jacobian optimization-based rezone strategies for arbitrary Lagrangian Eulerian methods. *Journal of Computational Physics*, 176:93–128, 2002.

[58] P. Knupp and S. Steinberg. *Fundamentals of Grid Generation*. CRC Press, Boca Raton, 1993.

[59] S. H. Lee, H. A. Tchelepi, P. Jenny, and L. J. DeChant. Implementation of a flux-continuous finite-difference method for stratigraphic hexahedron grids. *SPE Journal*, 9:267–277, 2002.

[60] O. P. Lødøen, H. Omre, L. J. Durlofsky, and Y. Chen. Assessment of uncertainty in reservoir production forecasts using upscaled flow models. 7th International Geostatistics Conference, Banff, Canada, Sept. 26 - Oct. 1, 2004.

[61] S. Mao and A. G. Journel. Generation of a reference petrophysical/seismic data set: the Stanford V reservoir. Stanford Center for Reservoir Forecasting Report, 1998.

[62] O. Mascarenhas and L. J. Durlofsky. Coarse scale simulation of horizontal wells in heterogeneous reservoirs. *Journal of Petroleum Science and Engineering*, 25:135–147, 2000.

[63] M. J. Mlacnik, L. J. Durlofsky, and Z. E. Heinemann. Dynamic flow-based PEBI grids for reservoir simulation. SPE paper 90009, presented at the SPE Annual Technical Conference & Exhibition, Houston, TX, Sept. 26-29, 2004.

[64] M. J. Mlacnik, A. W. Harrer, and Z.E. Heinemann. Locally streamline-pressure-potential-based PEBI grids. SPE paper 79684, presented at the SPE Reservoir Simulation Symposium, Houston, TX, Feb. 3-5, 2003.

[65] J. D. Moulton, J. E. Dendy, and J. M. Hyman. The black box multigrid numerical homogenization algorithm. *Journal of Computational Physics*, 142:80–108, 1998.

[66] A. H. Muggeridge, M. Cuypers, C. Bacquet, and J. W. Barker. Scale-up of well performance for reservoir flow simulation. *Petroleum Geoscience*, 8:133–139, 2002.

[67] B. F. Nielsen and A. Tveito. An upscaling method for one-phase flow in heterogeneous reservoirs. A Weighted Output Least Squares (WOLS) approach. *Computational Geosciences*, 2:93–123, 1998.

[68] A.E. O'Sullivan and M.A. Christie. Solution error models: a new approach for coarse grid history matching. SPE paper 93268, presented at the SPE Reservoir Simulation Symposium, Houston, TX, Jan. 31 - Feb. 2, 2005.

[69] D. W. Peaceman. *Fundamentals of Numerical Reservoir Simulation*. Elsevier, New York, 1977.

[70] D. W. Peaceman. Interpretation of well-block pressures in numerical reservoir simulation with nonsquare grid blocks and anisotropic permeability. *SPE Journal*, 23:531–543, 1983.

[71] G. E. Pickup, J. L. Jensen, P. S. Ringrose, and K. S. Sorbie. A method for calculating permeability tensors using perturbed boundary conditions. 3rd European Conference on the Mathematics of Oil Recovery, Delft, The Netherlands, 1992.

[72] G. E. Pickup, P. S. Ringrose, J. L. Jensen, and K. S. Sorbie. Permeability tensors for sedimentary structures. *Mathematical Geology*, 26:227–250, 1994.

[73] R. C. M. Portella and T. A. Hewett. Upscaling, gridding, and simulation using streamtubes. *SPE Journal*, 5:315–323, 2000.

[74] M. Prevost. *Accurate Coarse Reservoir Modeling Using Unstructured Grids, Flow-based Upscaling and Streamline Simulation*. Ph.D. thesis, Stanford University, Stanford, CA, 2003.

[75] M. Prevost, M. G. Edwards, and M. J. Blunt. Streamline tracing on curvilinear structured and unstructured grids. *SPE Journal*, 7:139–148, 2002.

[76] M. Prevost, F. Lepage, L. J. Durlofsky, and J.-L. Mallet. Unstructured 3D gridding and upscaling for coarse modeling of geometrically complex reservoirs. 9th European Conference on the Mathematics of Oil Recovery, Cannes, France, Aug. 30 - Sept. 2, 2004.

[77] M. Ramè and J. E. Killough. A new approach to the simulation of flows in highly heterogeneous porous media. SPE paper 21247, presented at the SPE Reservoir Simulation Symposium, Anaheim, CA, Feb. 17-20, 1991.

[78] Ph. Renard and G. de Marsily. Calculating effective permeability: a review. *Advances in Water Resources*, 20:253–278, 1997.

[79] R. K. Romeu and B. Noetinger. Calculation of internodal transmissivities in finite difference models of flow in heterogeneous porous media. *Water Resources Research*, 31:943–959, 1995.

[80] Y. Rubin and J. J. Gómez-Hernández. A stochastic approach to the problem of upscaling of conductivity in disordered media: theory and unconditional numerical simulations. *Water Resources Research*, 26:691–701, 1990.

[81] A. Saez, C. J. Otero, and I. Rusinek. The effective homogeneous behavior of heterogeneous media. *Transport in Porous Media*, 4:213–238, 1989.

[82] M. R. Thiele, R. P. Batycky, M. J. Blunt, and F. M. Orr. Simulating flow in heterogeneous systems using streamtubes and streamlines. *SPE Reservoir Engineering*, 11:5–12, 1996.

[83] J. F. Thompson, Z. U. A. Warsi, and C. W. Mastin. *Numerical Grid Generation: Foundations and Applications*. North-Holland, New York, 1985.

[84] T. T. Tran. *Stochastic Simulation of Permeability Fields and their Scale Up for Flow Modeling*. Ph.D. thesis, Stanford University, Stanford, CA, 1995.

[85] S. Verma and K. Aziz. A control volume scheme for flexible grids in reservoir simulation. SPE paper 37999, presented at the SPE Reservoir Simulation Symposium, Dallas, TX, June 8-11, 1997.

[86] X. H. Wen, L. J. Durlofsky, and Y. Chen. Efficient three-dimensional implementation of local-global upscaling for reservoir simulation. SPE paper 92965, presented at the SPE Reservoir Simulation Symposium, Houston, TX, Jan. 31 - Feb. 2, 2005.

[87] X. H. Wen, L. J. Durlofsky, and M. G. Edwards. Upscaling of channel systems in two dimensions using flow-based grids. *Transport in Porous Media*, 51:343–366, 2003.

[88] X. H. Wen, L. J. Durlofsky, and M. G. Edwards. Use of border regions for improved permeability upscaling. *Mathematical Geology*, 35:521–547, 2003.

[89] X. H. Wen, L. J. Durlofsky, S. H. Lee, and M. G. Edwards. Full tensor upscaling of geologically complex reservoir descriptions. SPE paper 62928, presented at the SPE Annual Technical Conference & Exhibition, Dallas, TX, Oct. 1-4, 2000.

[90] X. H. Wen and J. J. Gómez-Hernández. Upscaling hydraulic conductivities in heterogeneous media: an overview. *Journal of Hydrology*, 183:ix–xxxii, 1996.

[91] X. H. Wen and J. J. Gómez-Hernández. Upscaling hydraulic conductivities in cross-bedded formations. *Mathematical Geology*, 30:181–211, 1998.

[92] C. D. White and R. N. Horne. Computing absolute transmissibility in the presence of fine-scale heterogeneity. SPE paper 16011, presented at the SPE Reservoir Simulation Symposium, San Antonio, TX, Feb. 1-4, 1987.

[93] X. H. Wu, Y. R. Efendiev, and T. Y. Hou. Analysis of upscaling absolute permeability. *Discrete and Continuous Dynamical Systems, Series B*, 2:185–204, 2002.

[94] W. Zijl and A. Trykozko. Numerical homogenization of the absolute permeability using the conformal-nodal and the mixed-hybrid finite element method. *Transport in Porous Media*, 44:33–62, 2001.